

Summer Student Lecture Notes

INTERFEROMETRY AND APERTURE SYNTHESIS

Bruce Balick

July 1973

The following pages are reprinted  
(with corrections) from

Balick, B. 1972, thesis  
(Cornell University)

## CHAPTER II

### INTERFEROMETRY AND APERTURE SYNTHESIS

Electromagnetic radiation is a wave phenomena, consequently instruments used to observe this radiation are subject to diffraction limitations on their resolution. The angular limit,  $\Delta\theta$ , is given approximately by  $\Delta\theta \sim D/\lambda$ , where  $D$  is the aperture dimension and  $\lambda$  is the observing wavelength; for radio work

$$\frac{\Delta\theta}{\text{min arc}} = 140 \frac{[\lambda/\text{cm}]}{[D/\text{feet}]}$$

Thus the 300-foot telescope has a maximum resolution of  $\sim 6'$  arc at  $\lambda 11$  cm, whereas a 10-cm aperture optical telescope has a diffraction limit of  $1''$  arc at optical wavelengths. (The same high resolution would require apertures 1-1000 km in diameter at radio wavelengths.)

To obtain high resolution at radio wavelengths, partially filled apertures of large diameter can be synthesized. For this, two telescopes separated by a baseline  $B$  can be used to simulate the response of a nearly circular annulus of diameter  $|B|$ . The telescope pair is configured in such a manner that it is best described as an interferometer in the ordinary optical sense. By moving the telescopes to obtain interferometers of different spacings, annuli of different sizes can be simulated. The results obtained on the various spacings can be added appropriately to synthesize the response of a single telescope of very large diameter, and thereby yield maps of high resolution. For example, the interferometer of the National Radio Astronomy Observatory (NRAO) can

be used to synthesize an aperture of 2.7-km diameter. At a wavelength of 3.7 cm, the resolution is 3" arc.

Because the synthesized aperture is not completely filled, but rather consists of a series of elliptical annuli, the beam pattern used for the observations is complex. The beam can be described in terms of a "main beam" of half-power width (HPW) which depends on the maximum dimensions of the aperture, and a complex series of "side lobes" which arise mainly because the synthesized aperture is not filled. The response of the sidelobes for the NRAO instrument can be of order 10-20% of the main beam, depending on declination. Thus the maps produced by the aperture synthesis technique do not lend themselves to quantitative interpretation without careful analysis.

Since the present work depends heavily on results obtained through aperture synthesis, it will be necessary to present the theory of the method in some detail. Although the theory is mathematically complex, an intuitive understanding based on simple principles is possible. The first sections of this chapter are devoted to a simplified description of interferometry and aperture synthesis in order to understand the response of an idealized instrument to simple and complex sources. In order to provide a suitable background for understanding the present observations, it is also necessary to understand observing problems which arise in the case of the real (i.e., non-ideal interferometry).

In the later sections of the chapter we investigate the effects of noise and miscalibration. Finally, the process of constructing the map and problems associated with its calibration are presented. All

discussion is illustrated by reference to the NRAO interferometer which was used for the present observations.

Outline of Chapter II:

- A. General Principles
- B. Response to Complex Sources
- C. The Real Interferometer
- D. Error Analysis
- E. Constructing and Interpreting the Maps

A. GENERAL PRINCIPLES

An ideal interferometer consists of two identical telescopes joined by equal lengths of cable into a multiplier where the noiseless signals from both telescopes are multiplied (correlated). The ideal source is a stationary, monochromatic point source at infinity. We shall later relax some of these assumptions. The discussion which follows in this section has a close analogy in the case of the optical, double-slit interferometer.

The ideal interferometer is shown schematically in Figure II.1.  $\mathbf{B}$  is the vector baseline separation, measured in wavelengths. The specific coordinate system used to describe  $\mathbf{B}$  is not important and will be chosen for convenience later. The output voltages of the RF amplifiers of telescopes 1 and 2 are\*

$$\begin{aligned} V_1 &= \sqrt{1/2 A_e G} \epsilon \cos \left( 2\pi \frac{c}{\lambda} t \right) \\ &= V_{01} \cos (2\pi ft) \\ V_2 &= V_{02} \cos (2\pi ft + \phi) \end{aligned}$$

---

\* In the discussion which immediately follows, it is assumed (but is not essential) that the reader is familiar with the response of the electronics typically found on single-dish telescopes.

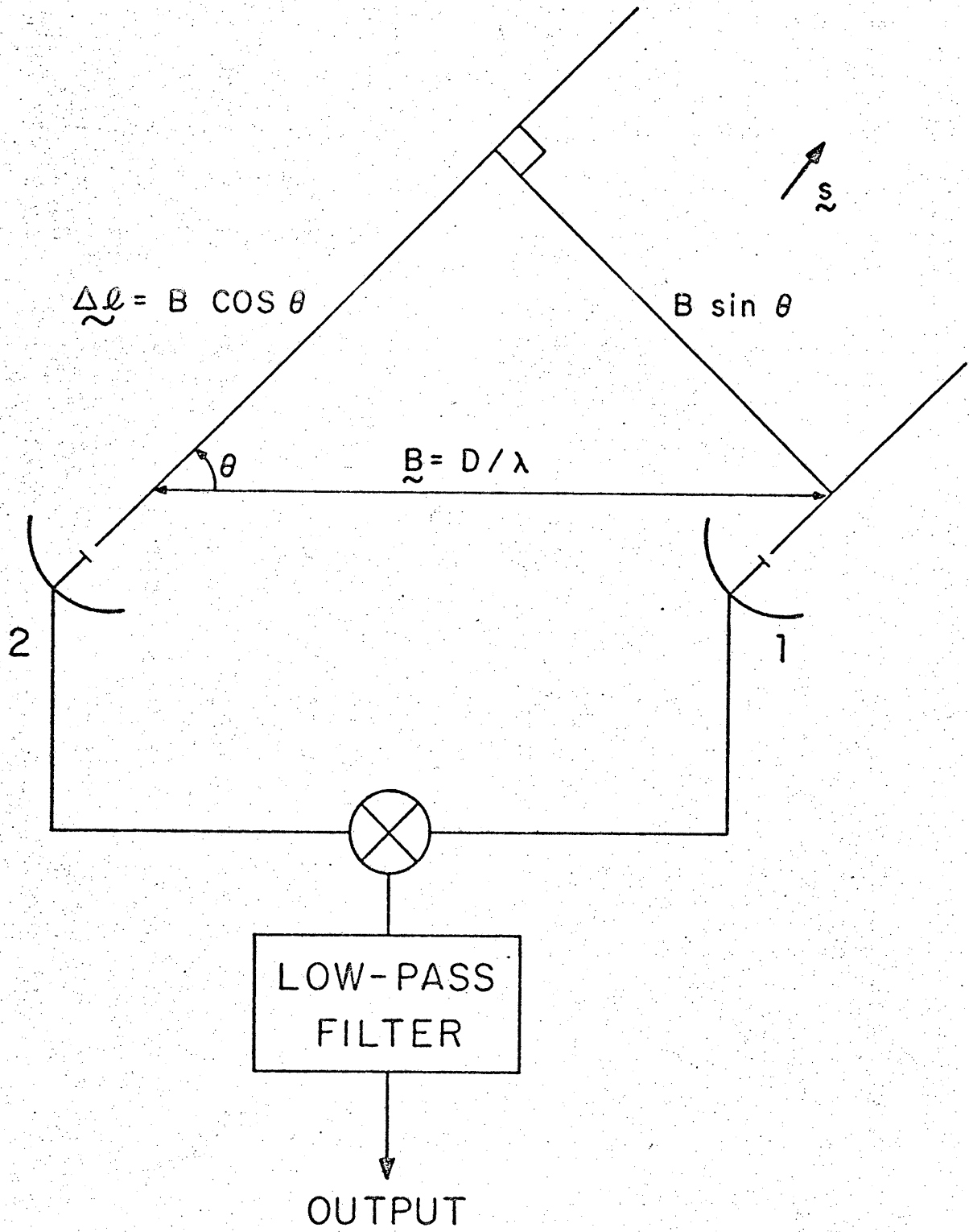


Figure II.1. The idealized interferometer.

where  $A_e$  is the effective area of the antenna,  $\epsilon$  is the strength of the incoming signal,  $G$  is the amplifier power gain,  $f$  is the observing frequency,  $V_{01}$  and  $V_{02}$  are the output voltages (assumed to be equal), and the  $1/2$  arises because we measure only one polarization.  $\phi = 2\pi \Delta\ell/\lambda$  is the lag of the signal from Telescope 2 arising because the path length from 2 is greater by an amount  $\Delta\ell = \underline{s} \cdot \underline{B} \cos \theta$  where  $\underline{s}$  is a unit vector in the direction of the source, and we let the magnitude of a vector " $\underline{x}$ " be represented by " $x$ ". The RF signals are mixed by a common local oscillator to obtain the IF signals which are then multiplied in the correlator. The multiplier output  $M$  is thus given by

$$\begin{aligned} M &= V_1 V_2 = V_o^2 \cos(2\pi f_{IF} t) \cos(2\pi f_{IF} t + \phi) \\ &= 1/2 V_o^2 [\cos \phi + \cos \{2\pi(2f_{IF})t + \phi\}]. \end{aligned}$$

The second term is a high-frequency signal which is rejected by the low-pass filter whose output  $R$  is thus proportional to  $V_o^2 \cos(2\pi \Delta\ell/\lambda)$ . If the source were stationary with respect to the baseline, this output would be a constant; however, because the source (as seen from the baseline) appears to move as the earth rotates,  $\Delta\ell$  changes by many wavelengths and the output varies nearly sinusoidally resulting in the characteristic "fringe" pattern (each fringe results from a change in  $\Delta\ell$  of one wavelength). The amplitude of the fringes is directly proportional to the source strength  $S$ , where  $S$  is the radio flux density of the source,

(II.1)

$$R \propto V_o^2 \cos [2\pi |\underline{B}| \cos \theta] \propto S \cos 2\pi \underline{B} \cdot \underline{s}.$$

This is the first fundamental equation of interferometry. Examples of fringes are shown in Figure II.2.

The interferometer response can be alternately pictured as a set of fixed sinusoidal lobes which are parallel but not quite equally spaced (the spacing is discussed below). The "comb" of lobes are schematically shown in various aspects in Figures II.3a, 3b, and 3c. Sources move through the comb as the earth rotates. The paths of sources at  $\delta = 0^\circ$ ,  $30^\circ$ , and  $60^\circ$  are shown. Also indicated is the tracking limit of the telescopes at hour angles of  $\pm 6^h$ . Note that the total number of lobes in the sky is  $2B$ , where  $B$  is measured in wavelengths. This follows since  $-B \leq B \cdot \xi \leq B$ .

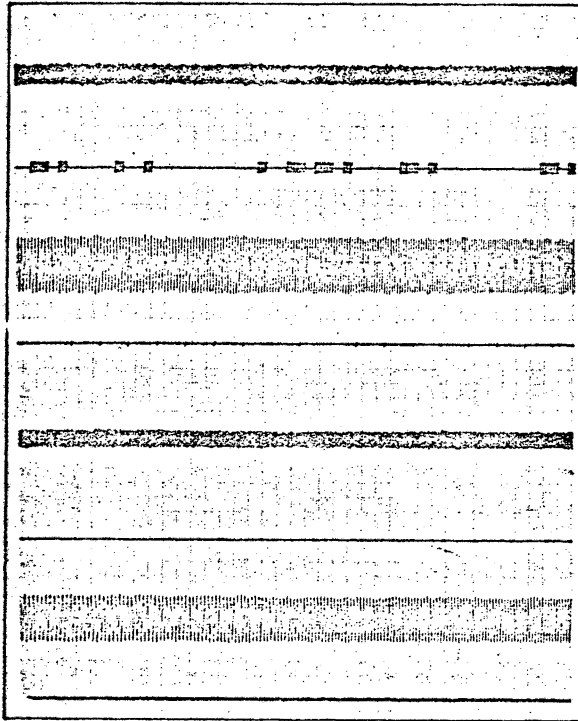
These lobes are not a property of the individual antennae, but only of their relative placement and their orientation with respect to the instantaneous direction of the source. To repeat, fringes are a result of the changing source-baseline geometry. They are independent of the observing frequency if  $B$  is measured in wavelengths. The primary antenna patterns of the single dish telescopes do not directly enter into the fringe pattern, but merely select a region of the sky over which radiation from sources moving through the lobes can be observed. Thus the individual antennae must track the source.

The lobe separation is the angular separation of adjacent lobe maxima,  $\Delta\theta$ .  $\Delta\theta$  is determined by the condition that  $2\pi B \cos \theta$  changes by  $2\pi$ . Let  $\theta_1$  and  $\theta_2$  be two angles for which  $B \cos \theta$  changes by unity; that is,

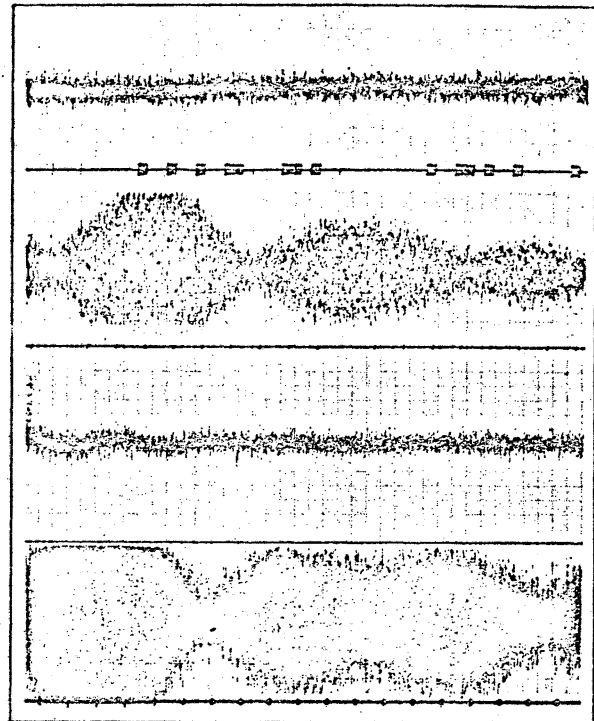
$$\theta_2 = \theta_1 + \Delta\theta$$

$$2\pi B (\cos \theta_1 - \cos \theta_2) = 2\pi$$

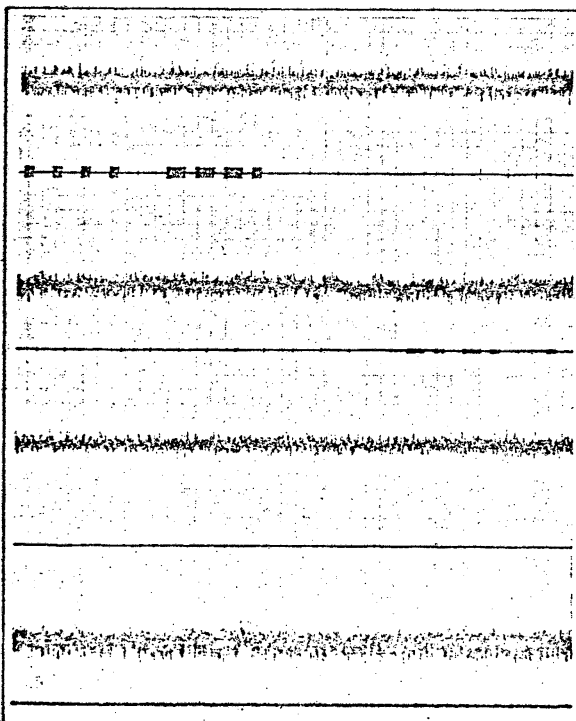
## EXAMPLES OF FRINGES



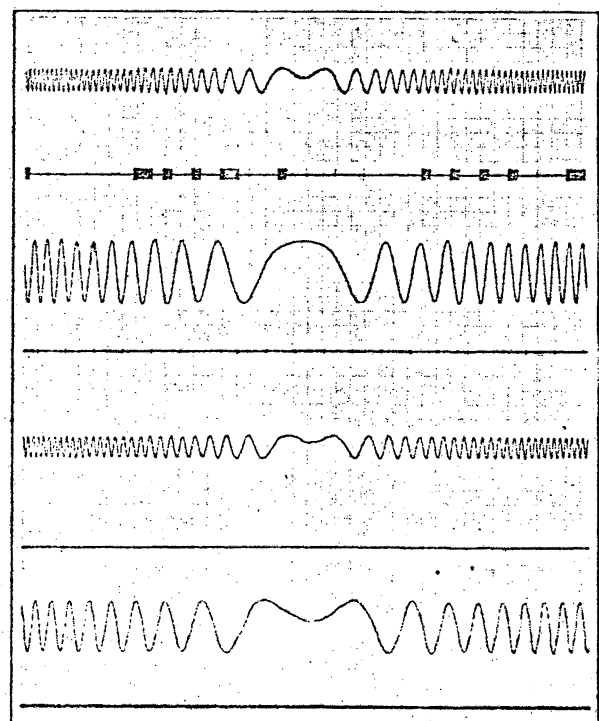
POINT SOURCE



COMPLEX SOURCE



WEAK SOURCE



CROSSOVER

Figure II.2. Examples of fringes.



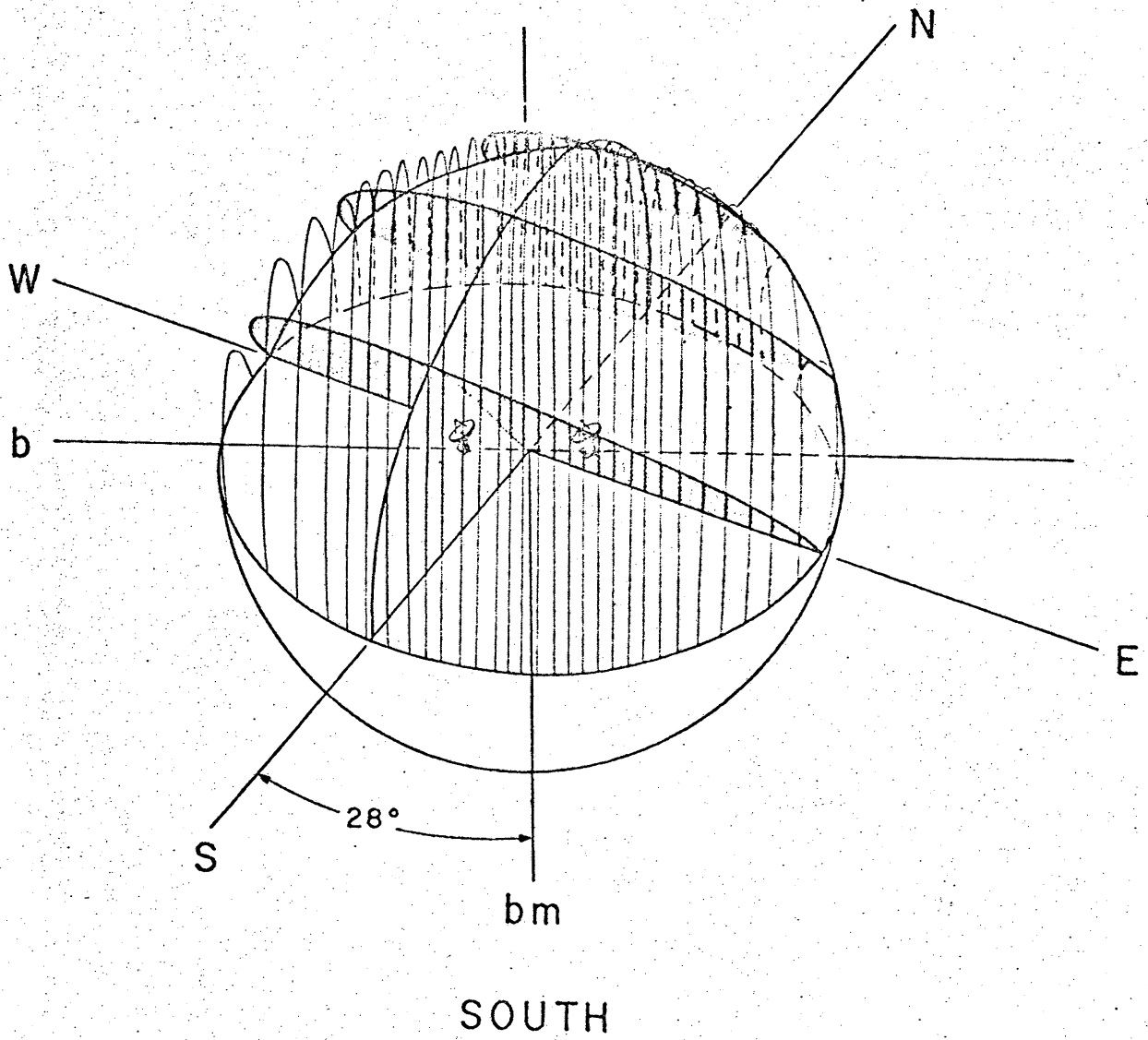


Figure II.3b. Lobe-source geometry viewed from the baseline meridian.

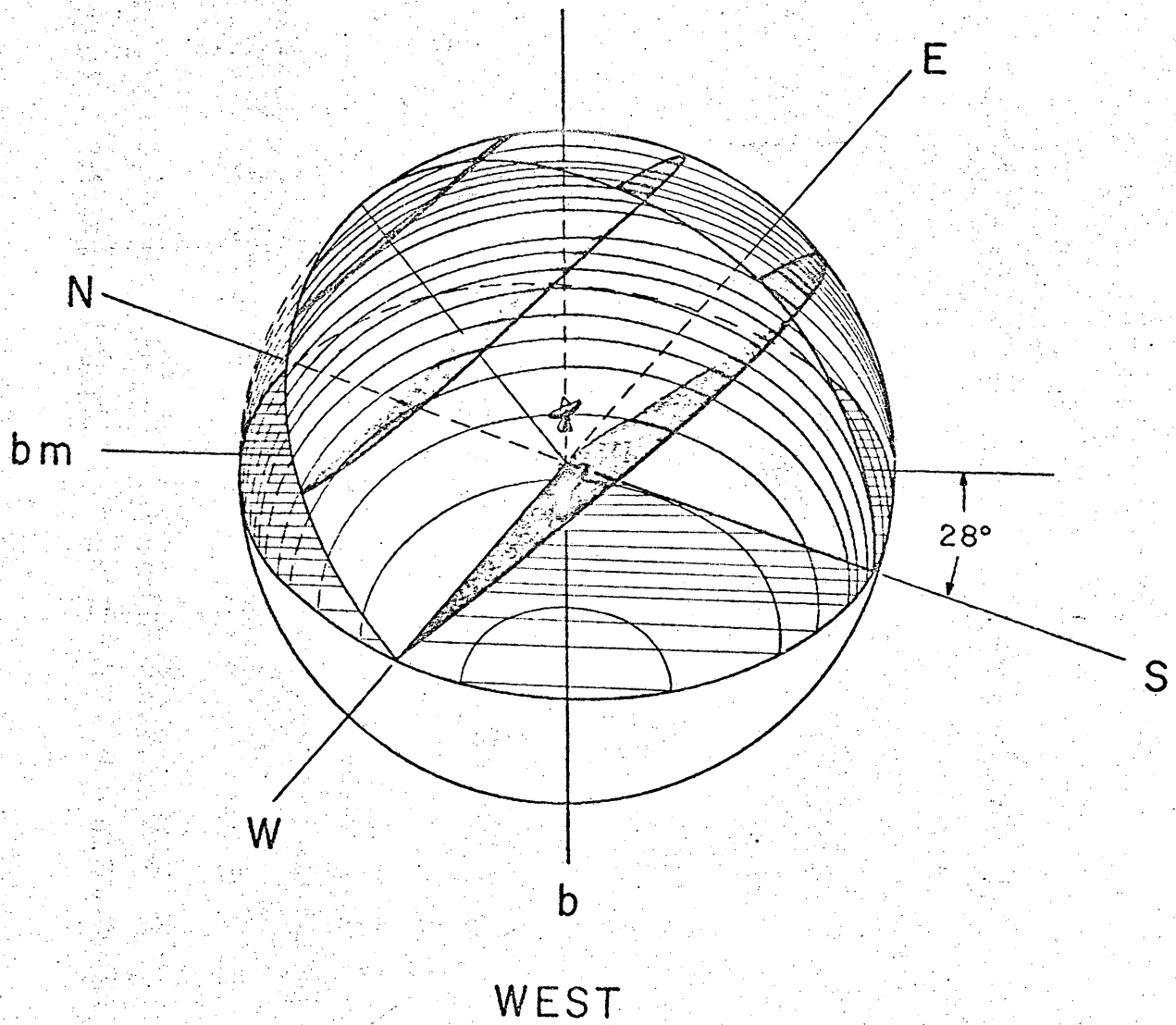


Figure II.3c. Lobe-source geometry viewed from the SW end of the baseline.

Then

(II.2)

$$\Delta\theta = \frac{1}{B \sin \theta} = \frac{1}{|B \times \xi|} \text{ radians}$$

which is the second basic equation of interferometry.  $B \times \xi$  is the component of the baseline which is perpendicular to the direction of the source. That is, as seen by the source, the lobe separation  $\Delta\theta$  is determined by the projected baseline length. The orientation of the lobes is always perpendicular to the projected baseline. Therefore, to the source, the lobes appear to rotate as the earth's rotation causes the baseline orientation to change (see, for example, Figure II.3c).

The minimum lobe separations (i.e., those available at the instrumental meridian where the effective baseline is the true baseline) are shown in Table II.1 for an observing wavelength of 11.1 cm on the NRAO interferometer.

TABLE II.1

Baseline (100 meters)	1	2	3	4	5	6	7	8
Lobe separation	3!8	1!9	1!3	57"	46"	38"	33"	28"
Baseline (100 meters)	9	12	15	18	19	21	24	27
Lobe separation	25"	19"	15"	13"	12"	11"	10"	8!5

When sources pass through the meridian of the baseline ( $b_m$ ), then the effective baseline, and thus the number of fringes traversed per unit time, is a maximum. Also, the lobe separation is a minimum. When the source crosses over the end of the baseline (called crossover), the baseline projection goes through a minimum. In addition, the source is

moving in a direction which is instantaneously parallel to the lobes, so no lobes are traversed, and the fringe rate instantaneously drops to zero. See Figures II.2 and II.3c.

Let us view the baseline from the source in order to define some important new variables. Imagine an observer fixed on the source who sees the baseline change below him as the earth rotates. The baseline, projected onto his sky, ascribes a smooth curve. He can measure an east-west and north-south component of the instantaneous baseline projection; call these  $u$  and  $v$ . The geometry is shown in Figure II.4. As the earth rotates, the baseline "turns" and  $u$  and  $v$  change. For sources nearly overhead, the ends of the baseline describe almost circular paths. These paths, for sources at different declinations, are shown in Figure II.5 for a possible baseline of the NRAO interferometer. The abscissa is  $u$  and the ordinate  $v$ . The baseline itself is shown in Figure II.6. Indicated on the figure are the possible telescope positions. Telescope separations of 1, 2, 3, 4, 5, 6, 7, 8, 9, 12, 15, 18, 19, 21, 24, and 27 hundred meters are possible. In Figure II.7 all the available projected baselines that can be seen by sources of different declinations are displayed. Ten divisions on the grid correspond to  $25,000\lambda$  at  $\lambda 11.1$  cm, and  $75,000\lambda$  at  $\lambda 3.7$  (the observing wavelengths of the NRAO instrument).

The graphs of Figure II.7 indicate all the spacings that a source at one of the declinations can see. This statement means exactly the same as the following:

The aperture which can be synthesized for the observation of a source at any declination is the sum total of all projected baselines as plotted in the  $u,v$  plane.

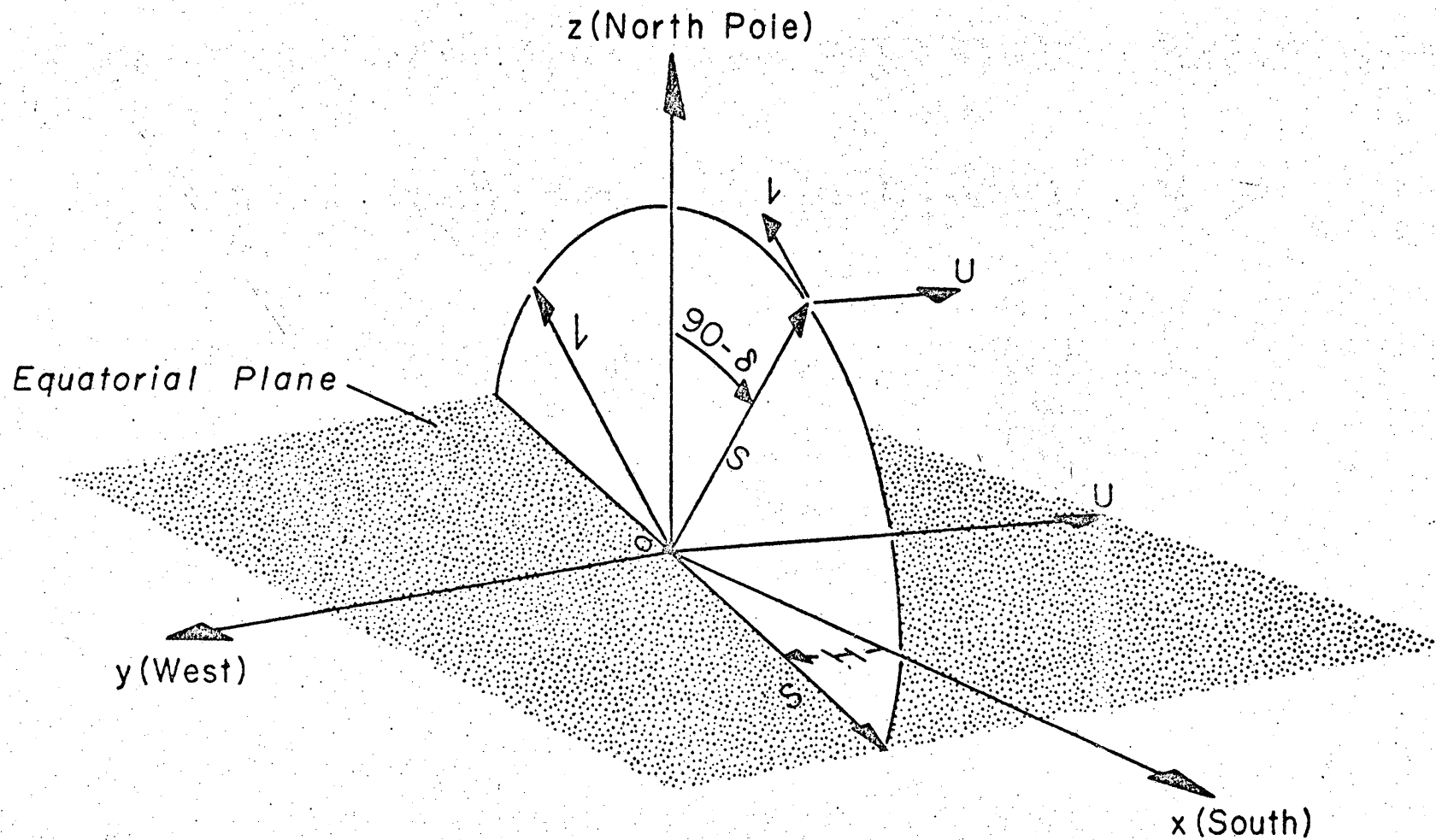


Figure II.4. Definitions of the  $(x, y, z)$  and  $(u, v)$  coordinate systems. The ground plane (not shown) intersects the equatorial plane along the  $y$  axis.

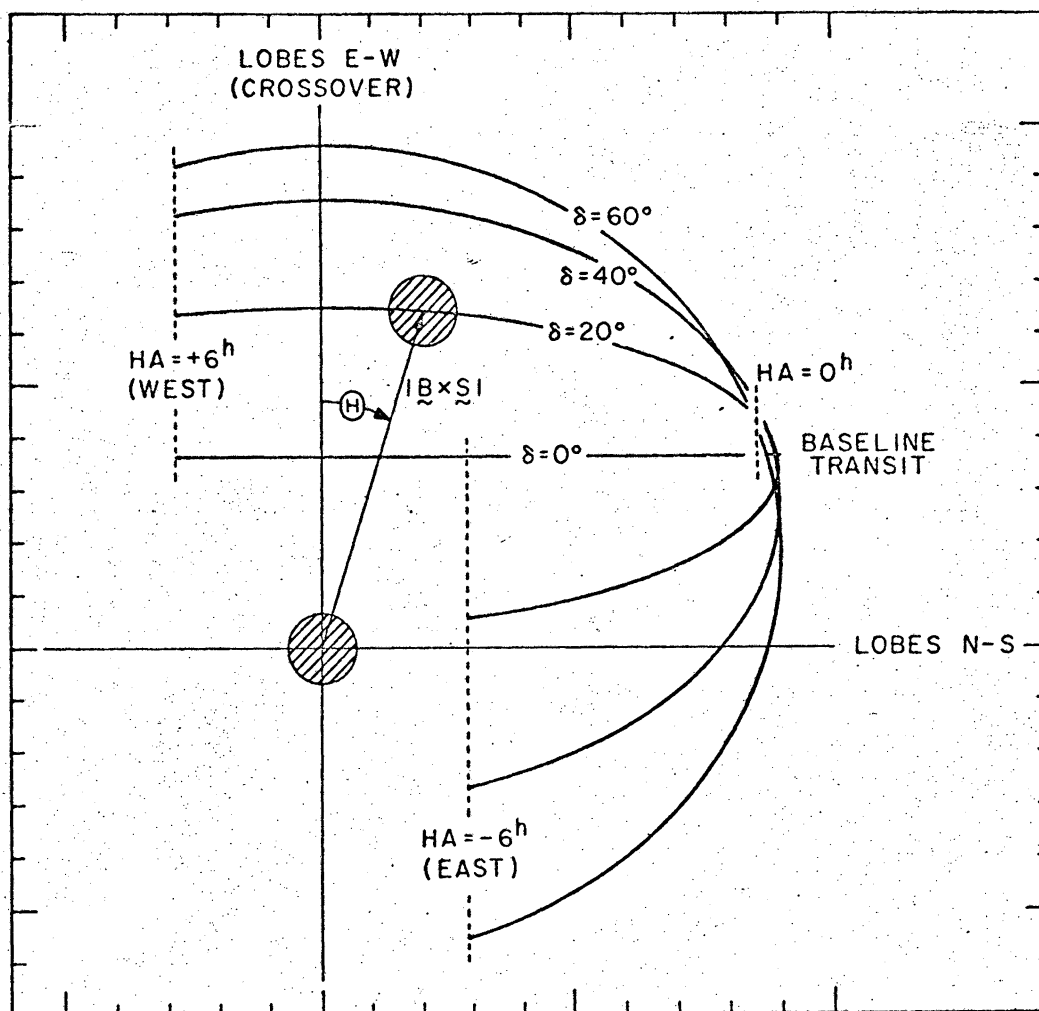


Figure II.5. The loci of projected baselines seen by sources at the indicated declinations as they move across the sky.

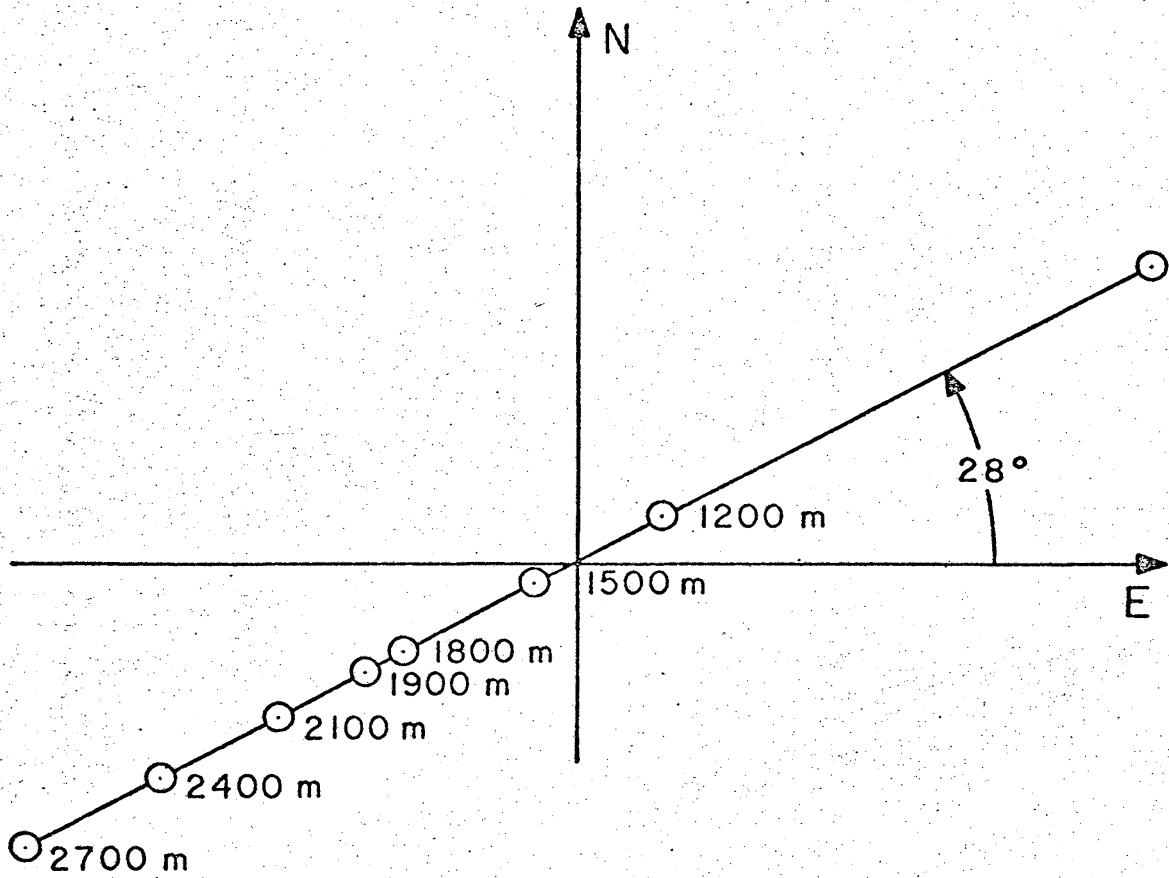


Figure II.6. The baseline and available telescope stations for the NRAO interferometer.

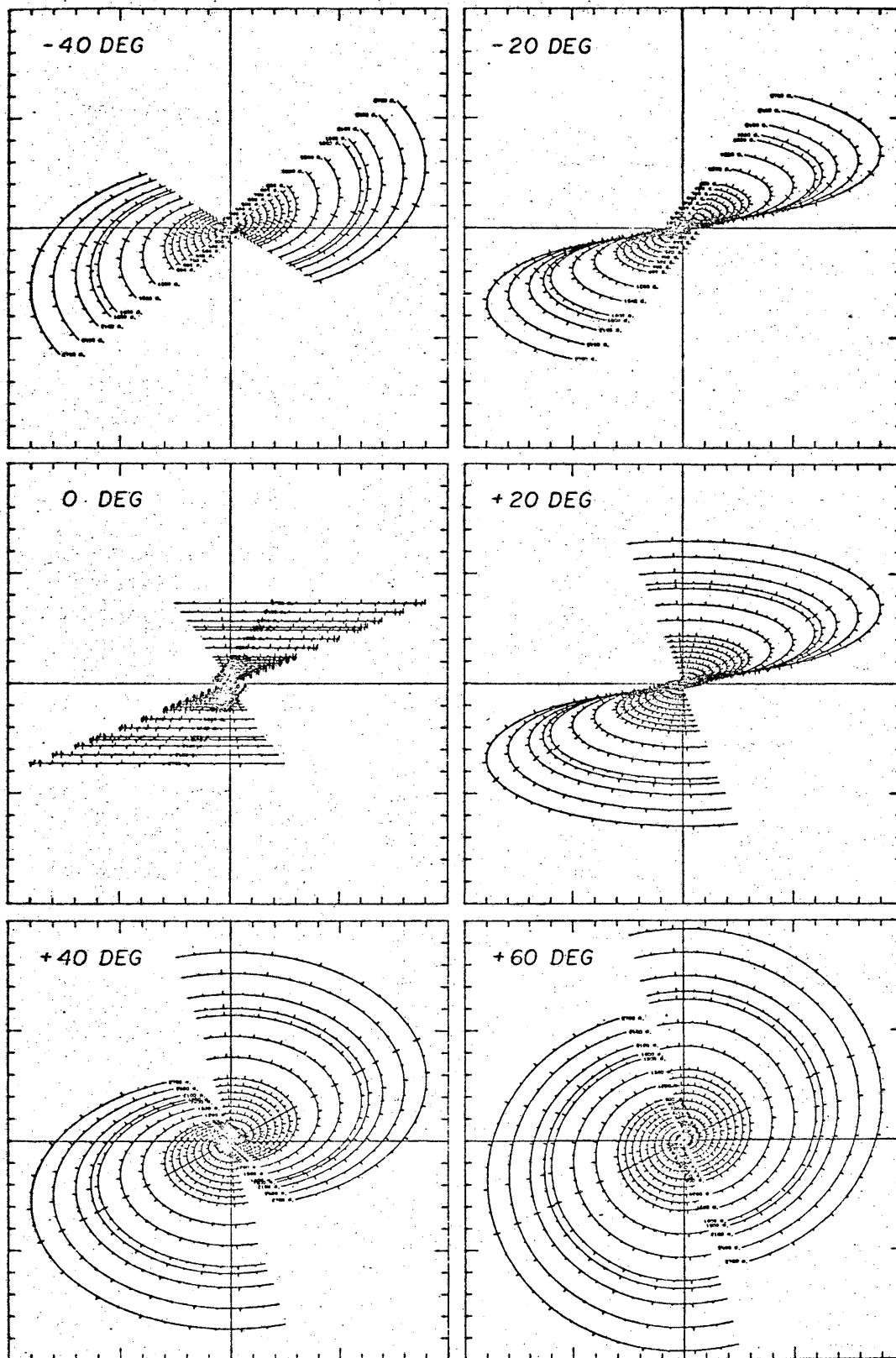


Figure II.7. The available baseline coverage, i.e., the synthesized aperture, for sources at the declinations indicated (for the NRAO interferometer). The distance between tick marks is 2500 wavelengths at  $\lambda 11.1$  cm (2695 MHz).

Thus the elliptical rings of Figure II.7 are a picture of the partially filled aperture which can be synthesized. It remains to be seen how the fringes observed at these points in the  $(u,v)$  plane can be used to construct a high-resolution map. For interest, the beam pattern of the synthesized aperture for sources at declinations of  $60^\circ$ ,  $30^\circ$ , and  $0^\circ$  are shown in Figures II.8a, b, and c. In Figure II.8d, the effect of neglecting the 600-meter spacing (arbitrarily chosen) on the synthesized beam is shown -- it is negligible.

It should be intuitively recognizable that  $u$  and  $v$  form a fundamental set of coordinates. Just how fundamental will be shown later. First we pause to establish some convenient coordinate systems so as to express  $u$  and  $v$  in terms of more intuitively obvious quantities like the hour angle  $H$ , the declination  $\delta$ , and the baseline length  $B$ . We shall also derive the equations for the elliptical annuli of Figure II.7.

We define a rectangular coordinate system which has components  $(x, y, \text{ and } z)$  along perpendicular directions in the equatorial plane and the North Pole. These directions are fixed with respect to the ground\*. The basic geometry of the  $(x, y, z)$  coordinate system is depicted in Figure II.4. The source, located in the direction of the vector  $\hat{s}$  has (changing) hour angle  $H$  and declination  $\delta$  as shown in the figure. The

---

\* That is, if  $\psi$  is the latitude of the observing site, then the baseline  $B_0$  on the ground has projections

$$\begin{pmatrix} B_x \\ B_y \\ B_z \end{pmatrix} = \begin{pmatrix} -\sin \psi & 0 & \cos \psi \\ 0 & -1 & 0 \\ \cos \psi & 0 & \sin \psi \end{pmatrix} \begin{pmatrix} B_{\text{north}} \\ B_{\text{east}} \\ B_{\text{zenith}} \end{pmatrix}$$

where  $B_{\text{zenith}}$  is 0 for baseline on level ground.

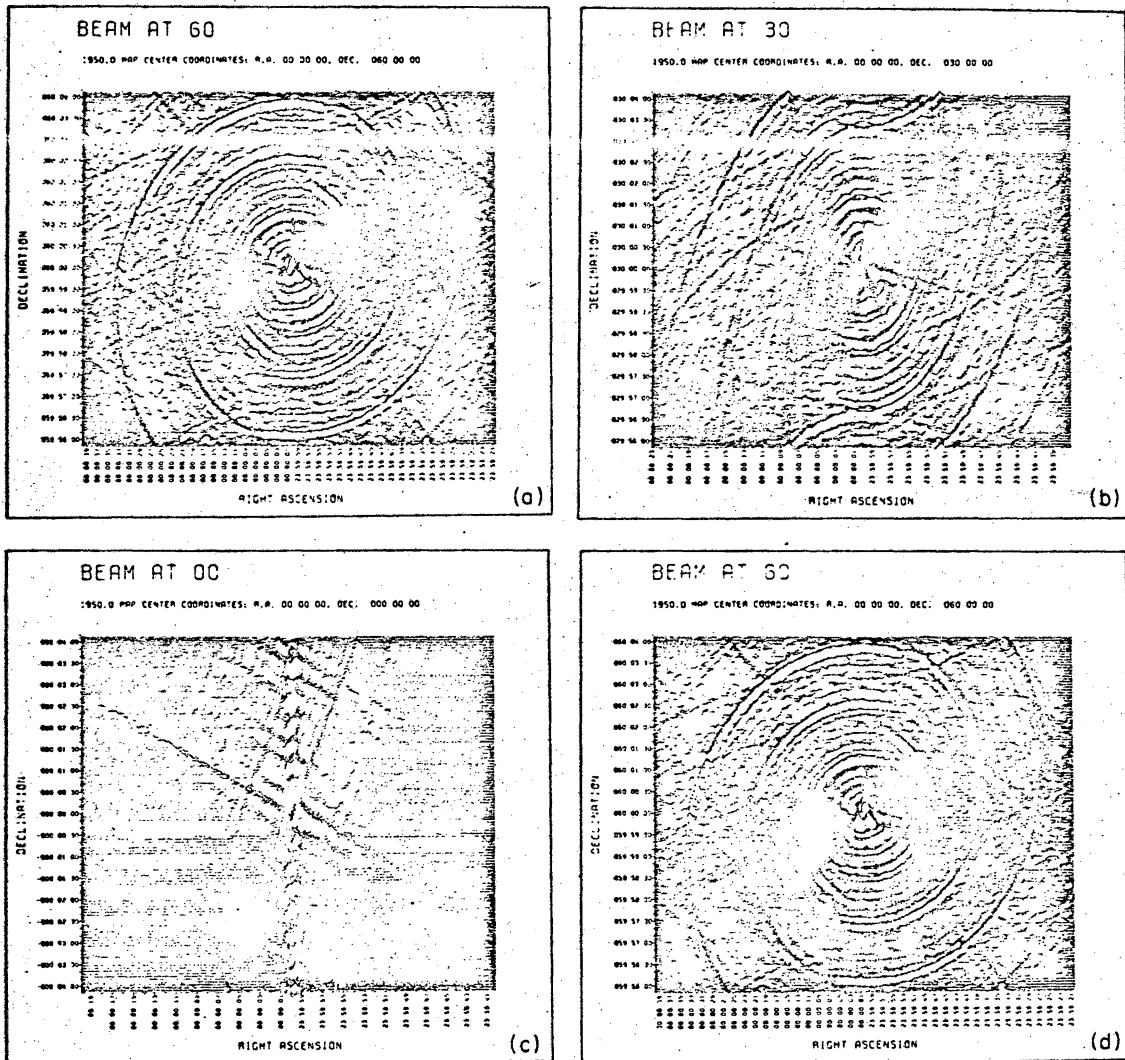


Figure II.8. The synthesized beams at  $\lambda = 0^\circ$ ,  $30^\circ$ , and  $60^\circ$ . The baseline coverage used for (d) was that of (a) except that the 600 m spacing was arbitrarily dropped.

baseline  $B$  would appear as a fixed line passing through the origin (but not necessarily in the  $(x,y)$  or equatorial plane). The baseline can also be defined by its length  $B$  and two fixed direction angles, called the baseline hour angle  $h$  and declination  $d$ . Then

$$\begin{pmatrix} B_x \\ B_y \\ B_z \end{pmatrix} = \begin{pmatrix} B \cos d \cos h \\ B \cos d \sin h \\ B \sin d \end{pmatrix} \quad \text{and} \quad \begin{pmatrix} s_x \\ s_y \\ s_z \end{pmatrix} = \begin{pmatrix} \cos \delta \cos H \\ \cos \delta \sin H \\ \sin \delta \end{pmatrix},$$

and  $\cos \theta = \hat{B} \cdot \hat{s} / B = \sin d \sin \delta + \cos d \cos \delta \cos (H-h)$ . The projected baseline  $B_x \times s_y$  changes with hour angle, but can at any time be resolved into its  $u,v$  components (perpendicular to the line of sight) as shown in the figure. By inspection

$$\begin{pmatrix} u \\ v \\ \Delta l \end{pmatrix} = \begin{pmatrix} \sin H & -\cos H & 0 \\ -\sin \delta \cos H & -\sin \delta \sin H & \cos \delta \\ \cos \delta \cos H & \cos \delta \sin H & \sin \delta \end{pmatrix} \cdot \begin{pmatrix} B_x \\ B_y \\ B_z \end{pmatrix}$$

Here  $\Delta l = \hat{B} \cdot \hat{s}$  is the component of the baseline along the line of sight. These matrix representations of the geometry were developed by Dr. C. M. Wade.

It can easily be verified that

$$\frac{u^2}{a^2} + \frac{(v - v_0)^2}{b^2} = 1$$

where  $a = \sqrt{B_x^2 + B_y^2} = B \cos d$ ,  $b = a \sin \delta = B \cos d \sin \delta$ , and

$v_0 = B_z \cos \delta = B \sin d \cos \delta$ . This is the equation of an ellipse centered at ( $u = 0$ ,  $v = -B \sin d \cos \delta$ ) with major axis  $a$ , minor axis  $b$ , and eccentricity  $\cos \delta$ . Note that only the minor axis and ellipse center depend on the source position.

#### B. RESPONSE TO COMPLEX SOURCES

It is the purpose of this section to establish the relationship between the observed fringe pattern and the source brightness distribution and to describe how the high-resolution map is obtained. We must first define those parameters that describe the observed fringe pattern and show, in a semi-intuitive fashion, how they relate to the source geometry. The precise relation between the source structure and interferometer response will then be developed.

The low-pass filter output  $R$  (i.e., the fringe pattern) can be written as

$$(II.3) \quad R = A \cos (2\pi B_z s + \phi),$$

where  $A$  is called the fringe amplitude (or colloquially, the amplitude),  $\phi$  is the fringe phase, or phase, and  $2\pi B_z s$  is the fringe period which is entirely a property of the source-earth geometry and has nothing to do with source structure. As a matter of procedure, the amplitude and phase are computed by an on-line computer (every 30 sec in the case of the NRAO interferometer) by a least squares fit to a sine wave of the expected period. The amplitude is the height of the fringes, and the phase is defined as the shift of the measured fringes with respect to the fringe pattern that would result from an ideal point source at

the same position in the sky. We now discuss the meaning of the amplitude and phase in more detail.

The amplitude, as we have established, is proportional to the flux of a point source. This, however, is not the case for an extended source. Consider now an extended source, say one of uniform brightness, that is sufficiently large that it spans more than one lobe, say  $N$  lobes. As the source moves through the lobes, it occupies all except perhaps one of them at any time. Compare this to a point source of the same flux  $S$  which would occupy either zero or one lobe. If the energy output of the low-pass filter for the point source is proportional to  $S$  for the point source, then it would be of order  $S \times [N - (N-1)]/N = S/N$  for the uniform extended source. In general, the larger the ratio of source size to lobe separation, the smaller the observed amplitudes for sources of the same flux.

Say many parallel pairs of telescopes of different separations simultaneously observe the same source. It follows that the amplitudes observed on the smaller spacings will be larger than those of the outer spacings for a source which is sufficiently extended. If the response to a source is found to fall off at a certain spacing, the source is said to be "resolved" at that spacing; otherwise it is unresolved. A plot of amplitude vs. spacing is called the real visibility function (this, we shall see, is a slight misnomer). Variations in this function are related to source structure; however, the real visibility function is not sufficient information from which to unambiguously derive a map of the source. The fringe phases clear up any ambiguities.

The meaning of the fringe phase is somewhat more esoteric. The phase is related to the apparent instantaneous brightness centroid offset from the center of the field of view; i.e., it is sensitive to position (this description of the phases has severe limitations). Consider a point source whose position is well known (to a small fraction of the lobe separation). Its fringe pattern has zero phase. Now displace the source a fraction of a lobe separation. The measured fringe pattern will have the same period (actually  $\xi$  changes slightly, but any differences in the period can generally be ignored); however, the fringes will not arrive at the expected time. If the source is displaced by half a lobe, the fringe phase will be  $180^\circ$ . If the source is displaced by an angular distance  $\Delta\theta$  and the lobe separation is  $\Delta\phi$ , the phase (in radians) will be  $2\pi \Delta\phi/\Delta\theta$ . Here it was assumed that the displacement of the source was along a line perpendicular to the lobes (see Figure II.9a).

As the source moves through the sky, it sees the baseline orientation, and thus the lobe orientation rotate slowly. Then the displacement of the displaced point source, projected onto a line perpendicular to the lobes, also changes; the phases change accordingly (see Figure II.9b). Then the response  $R$  is given by  $A \cos \{2\pi B \cdot (\xi + \Delta\xi)\}$  or  $\phi = 2\pi B \cdot \Delta\xi$ , where  $\Delta\xi$  is the source displacement. Letting the displacement have E-W components  $\Delta\alpha \cos \delta$  and N-S component  $\Delta\delta$ , and recalling the definition of  $u$  and  $v$ , we obtain

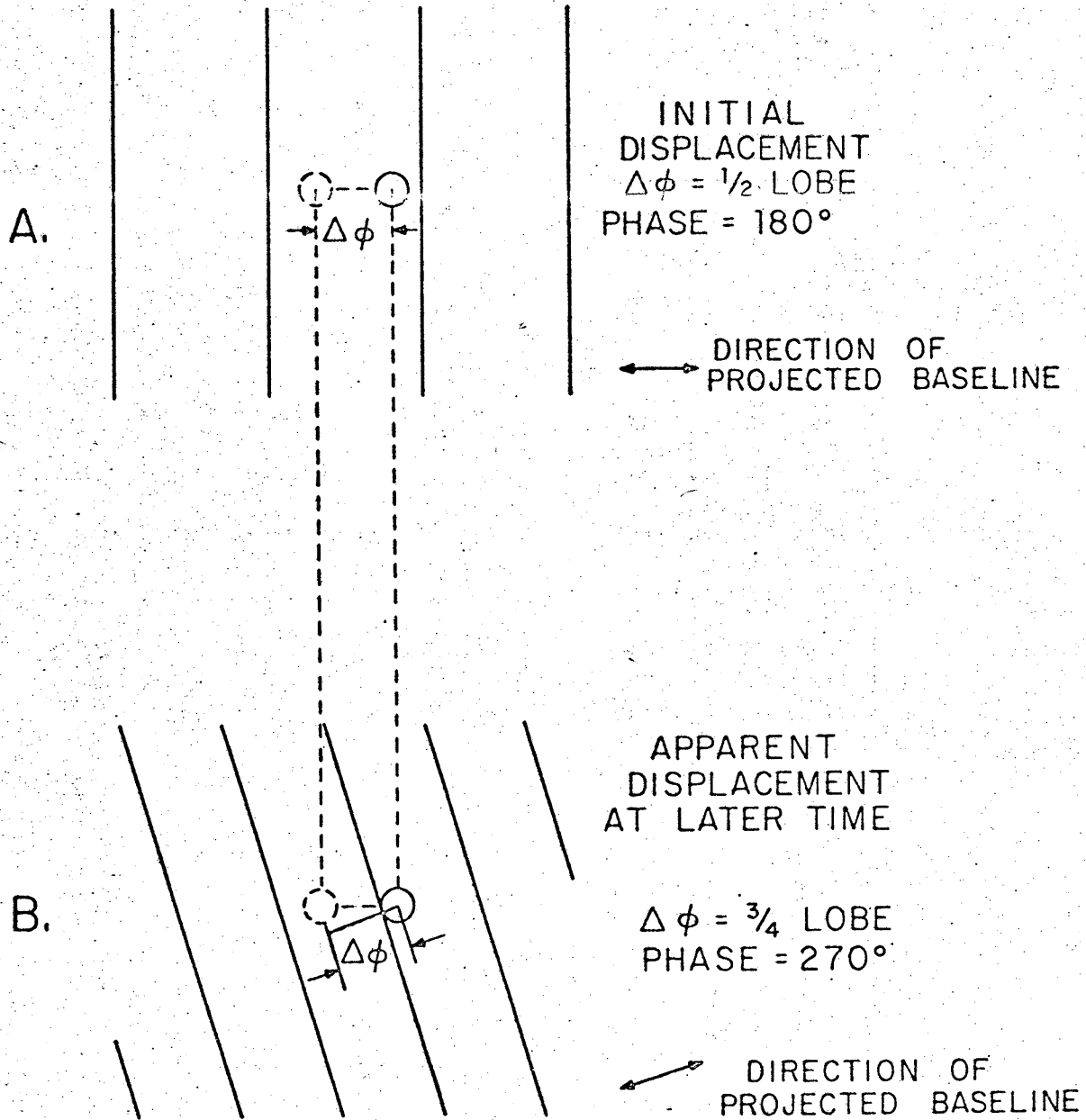


Figure II.9. A. Displacement of a point source (see text).  
B. Displacement of a point source viewed at a later time (see text).

$$\begin{aligned}
\phi(H, \delta) &= u \cdot \Delta\alpha \cos \delta + v \cdot \Delta\delta \\
&= \Delta\alpha (B_x \cos \delta \sin H - B_y \cos \delta \cos H) \\
&\quad + \Delta\delta (-B_x \sin \delta \cos H - B_y \sin \delta \sin H + B_z \cos \delta).
\end{aligned}$$

Note this implies that the phases can be represented as a flat plane which intersects the  $(u, v)$  plane along the line  $u \cdot \Delta\alpha \cos \delta + v \cdot \Delta\delta = 0$ . The phase behavior as the  $(u, v)$  ellipse is tracked is easily understood.

An identical discussion pertains to the phase of an extended source with symmetry such that its brightness centroid always appears stationary. This includes sources with circular symmetry and double sources (if the amplitudes are allowed to be negative -- see below). For very irregular sources the apparent brightness centroid changes erratically with a corresponding irregular phase behavior. See Figure II.10.

Having laid an intuitive groundwork for understanding the fringe amplitude and phase, we now show that both uniquely define a map and, in addition, we show how to construct the map. Consider an extended source contained well within the primary antennae beams. Let its brightness distribution be  $T(\alpha, \delta)$ . Let  $\alpha_0$  and  $\delta_0$  denote a reference position near the source -- say the center of the primary beam. We can define cartesian coordinates  $(x, y)$  in the plane of the sky with origin at  $(\alpha_0, \delta_0)$  with  $x = (\alpha - \alpha_0) \cos \delta_0$  and  $y = (\delta - \delta_0)$  (then  $x$  and  $y$  are not scaled by  $\cos \delta$  as  $\alpha$  and  $\delta$  are). An infinitesimal area in the source has intensity  $T(x, y) dx dy$ . The interferometer response to this element alone is identical to that of a point source located at an angle  $\theta$  with respect to the baseline:

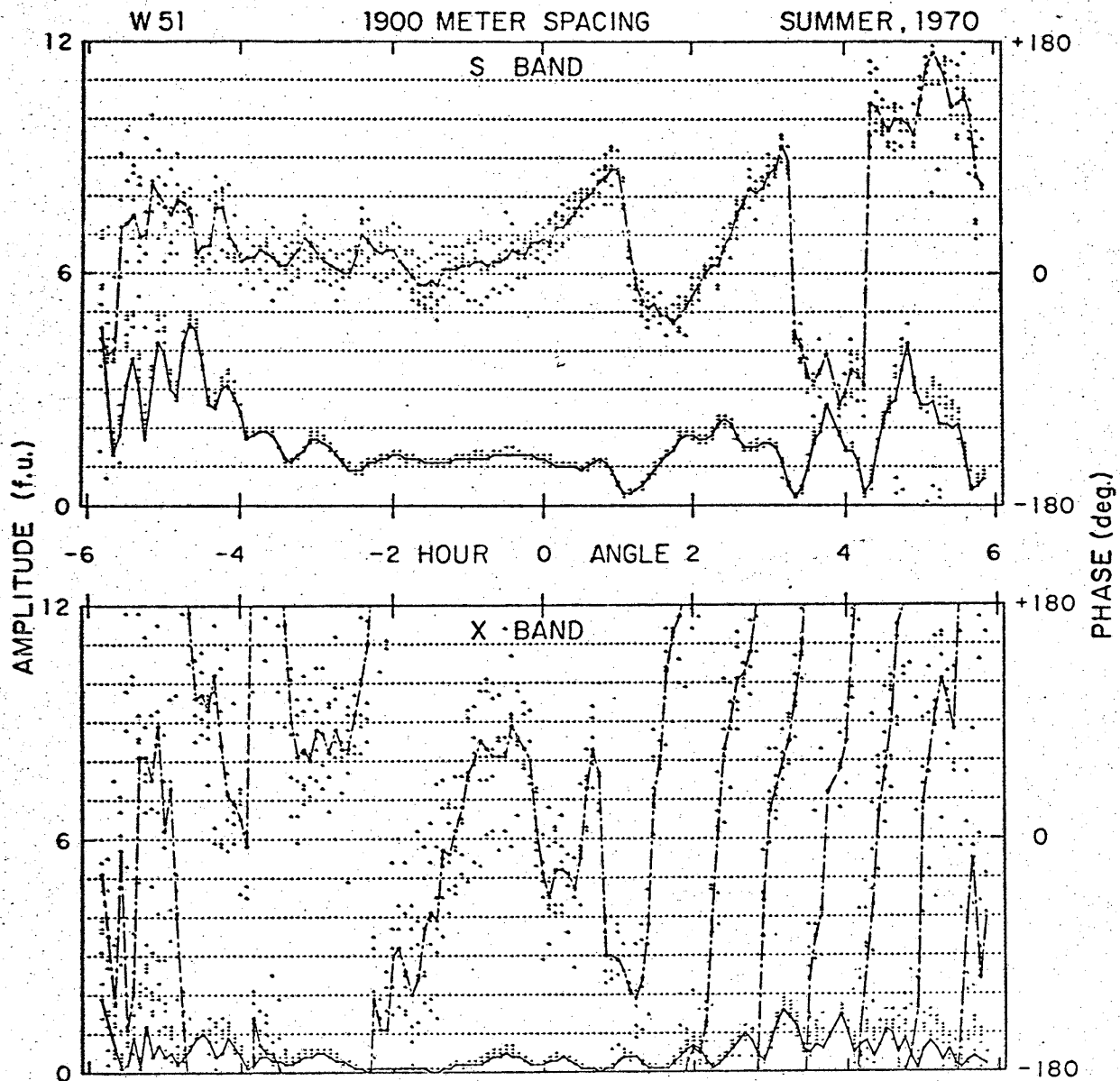


Figure II.10. Response of an interferometer to a complex source. Six independent observations are shown. Individual values of the amplitudes and phases ("A" and "P") as well as their vector averages (solid and broken lines) are indicated. S band is  $\lambda 11.1$  cm (2695 MHz); X band is  $\lambda 3.7$  cm.

$$dR \propto T(x,y) \cos (2\pi B \cos \theta) dx dy.$$

As stated previously, we may assume that the source dimensions are small so that the period of the fringes are the same over the entire source. This allows us to write the argument of the cosine in the form of equation II.3

$$dR \propto T(x,y) \cos \{2\pi B \cos \theta_0 + 2\pi (ux+vy)\}$$

where  $\theta_0$  is the angle between the baseline and the  $(x,y)$  origin (i.e.,  $B \cdot \xi = B \cos \theta_0$ ), and the phase  $\phi = 2\pi B \cdot \Delta s = 2\pi(ux+vy)$ . The same equation can be derived by a Taylor expansion of  $\cos \theta$  about the origin. For simplicity let us define  $\phi_0 = 2\pi B \cos \theta_0$ . Then expanding the cosine of a compound angle, we obtain

$$dR(u,v) \propto T(x,y) dx dy \{ \cos [2\pi(ux+vy)] \cos \phi_0 - \sin [2\pi(ux+vy)] \sin \phi_0 \},$$

Integrating over the source, we obtain the total response,

$$(II.4) \quad R(u,v) \propto S \{ \mathcal{R}(u,v) \cos \phi_0 - \mathcal{I}(u,v) \sin \phi_0 \},$$

where  $\mathcal{R}$  and  $\mathcal{I}$  are the normalized cosine and sine Fourier transforms of the source brightness distribution.

$$\begin{Bmatrix} \mathcal{R} \\ \mathcal{I} \end{Bmatrix} = \frac{1}{S} \frac{2k}{\lambda^2} \int_{-\infty}^{\infty} \int_{-\infty}^{\infty} T(x,y) \begin{Bmatrix} \cos \\ \sin \end{Bmatrix} [2\pi(ux + vy)] dx dy.$$

Here  $S$  is the usual flux density given by  $\frac{2k}{\lambda^2} \int_{-\infty}^{\infty} \int_{-\infty}^{\infty} T(x,y) dx dy$ . Note for a point source  $\mathcal{R} = 1$  and  $\mathcal{I} = 0$  resulting in equation II.1.

Because  $T(x,y)$  is a real function, so are  $R$  and  $I$ . We can therefore define the complex visibility function  $\mathcal{V}(u,v) \equiv \mathcal{R}(u,v) + i\mathcal{I}(u,v)$ , where  $R$  and  $I$  are its real and imaginary components. We can alternatively express  $\mathcal{V}$  in terms of an amplitude and phase,

$$(II.5) \quad \mathcal{V}(u,v) \equiv A(u,v) e^{i\phi(u,v)}$$

It follows that

$$A(u,v) = \sqrt{\{\mathcal{R}^2(u,v) + \mathcal{I}^2(u,v)\}},$$

and

$$\phi(u,v) = \tan^{-1} \frac{\mathcal{I}(u,v)}{\mathcal{R}(u,v)}$$

We can formally substitute these relations into equation (4):

$$\begin{aligned} R &\propto \{\mathcal{R}^2 + \mathcal{I}^2\}^{1/2} \left[ \frac{\mathcal{R}}{\{\mathcal{R}^2 + \mathcal{I}^2\}^{1/2}} \cos \phi_0 - \frac{\mathcal{I}}{\{\mathcal{R}^2 + \mathcal{I}^2\}^{1/2}} \sin \phi_0 \right] \\ &= A(u,v) \{\cos \phi \cos \phi_0 - \sin \phi \sin \phi_0\}, \text{ or} \end{aligned}$$

(II.6)

$$R \propto A(u,v) \cos \{2\pi \frac{B \cdot s}{\lambda} + \phi(u,v)\}$$

which is identical to equation II.3. Then the mathematically defined functions  $A$  and  $\phi$  take on a physical significance as the fringe amplitude and phase. That is, the fringe amplitude and phase are the amplitude and phase of the complex visibility function  $\mathcal{V}(u,v)$ , which itself is built from the Fourier sine and cosine transform of the brightness

distribution. A much clearer interpretation results from some last algebraic manipulation; from the definition of  $V$ ,  $R$ , and  $I$  we have,

$$V = R + iI = \frac{1}{S} \int_{-\infty}^{\infty} \int_{-\infty}^{\infty} T(x,y) \{ \cos 2\pi (ux+vy) + i \sin 2\pi (ux,vy) \} dx dy,$$

or

(II.7)

$$V(u,v) = \frac{1}{S} \int_{-\infty}^{\infty} \int_{-\infty}^{\infty} T(x,y) e^{2\pi i(ux+vy)} dx dy.$$

Then from the theory of the Fourier transform, we may write

THE MEASURED QUANTITIES OF THE INTERFEROMETER, THE FRINGE AMPLITUDE AND PHASE, FORM A COMPLEX FUNCTION  $V(u,v) = A(u,v) \exp (i\phi(u,v))$  WHOSE FOURIER TRANSFORM IS THE BRIGHTNESS DISTRIBUTION.

The interferometer then responds to Fourier components of the brightness distribution which have angular periods equal to the lobe separation and whose structure is oriented along a line perpendicular to the lobes. This is the fundamental principle of aperture synthesis. The source structure to which the interferometer responds is clearly defined, and we have shown that the brightness distribution can be constructed from the fringe amplitude and phase. The fundamental importance of  $u$  and  $v$  is also clear.

From equation II.7 we derive several corollaries which are important. Using the fact that  $T(x,y)$  is real and Fourier transform theory, we derive the following

$$\begin{aligned}
T(x,y) &= S \iint_{-\infty}^{\infty} \chi(u,v) \exp \{2\pi i(ux+vy)\} \, dudv \\
&= S \iint_{-\infty}^{\infty} \{R(u,v) \cos 2\pi(ux+vy) + I(u,v) \sin 2\pi(ux+vy)\} \, dudv \\
&\quad - iS \iint_{-\infty}^{\infty} \{R(u,v) \sin 2\pi(ux+vy) - I(u,v) \cos 2\pi(ux+vy)\} \, dudv \\
&= \iint_{-\infty}^{\infty} \{R(u,v) - R(-u,-v)\} \sin 2\pi(ux+vy) \, dudv \\
&\quad - \iint_{-\infty}^{\infty} \{I(u,v) + I(-u,-v)\} \cos 2\pi(ux+vy) \, dudv \\
&= 0,
\end{aligned}$$

where we have used the parity of the trigonometric functions and the fact that the imaginary part of  $T(x,y)$  is 0. Then

$$\begin{aligned}
R(u,v) &= R(-u,-v) \text{ and } I(u,v) = -I(-u,-v), \text{ or} \\
\chi(u,v) &= \chi^*(-u,-v),
\end{aligned}$$

where \* denotes complex conjugation. Thus the complex visibility function is said to be "Hermitian". It follows that  $A(u,v) = A(-u,-v)$  and  $\phi(u,v) = -\phi(-u,-v)$ , i.e., the amplitudes and phases are redundant on the  $(u,v)$  plane. Thus observations need only be taken over half the  $(u,v)$  plane. This is why the ellipses in Figure II.7 have counterparts on the opposite side of the origin.

Secondly, we note that  $S \cdot \chi(0,0) = \int T(x,y) \, dx \, dy = S$ . That is, the total flux of the source (which is assumed to be contained within the beam) is given by the zero spacing flux (at which all sources are unresolved). However, a physical telescope separation of zero is not possible. Even if the projected baseline falls to zero, then one

telescope occults the other. Thus the (u,v) origin cannot be sampled. Therefore the interferometer cannot be used to measure the total flux of a source unless the source is unresolved at some longer spacing. The failure to sample this point also means that the integral of the brightness temperature over any map must be 0; that is, the average brightness is zero and any source observed in the map forces some regions of the map to have negative temperatures. This means that negative sidelobes can appear on the map. Negative features in a map are not necessarily the result of noise, but are actually an inherent by-product of the aperture synthesis technique.

The response of the interferometer to model brightness distributions is shown in Figure II.11. Shown are five model Gaussian sources of the HPW's indicated (the beam can be considered as zero width Gaussian). The source intensities that will be observed on the NRAO interferometer are plotted on the right as a function of available telescope spacing (for an observing wavelength of 11.1 cm).  $\xi$  is the ratio of source to beam peak brightnesses, that is,  $\xi = \frac{[T_{\max} \text{ (extended source)}]}{[T_{\max} \text{ (point source)}]}$ , where  $T_{\max}$  is the peak source response. For this study the aperture was assumed to consist of circular annuli centered at the origin. This enabled the two-dimensional Fourier transform to be reduced to a one-dimensional radial integral.

The illustration highlights several very important effects. Note that for extended sources ( $\lambda \sim 1'$ ) how the rapidly decreasing visibility function is undersampled. In effect, such sources are observed on the innermost spacings only. The relatively large sidelobes

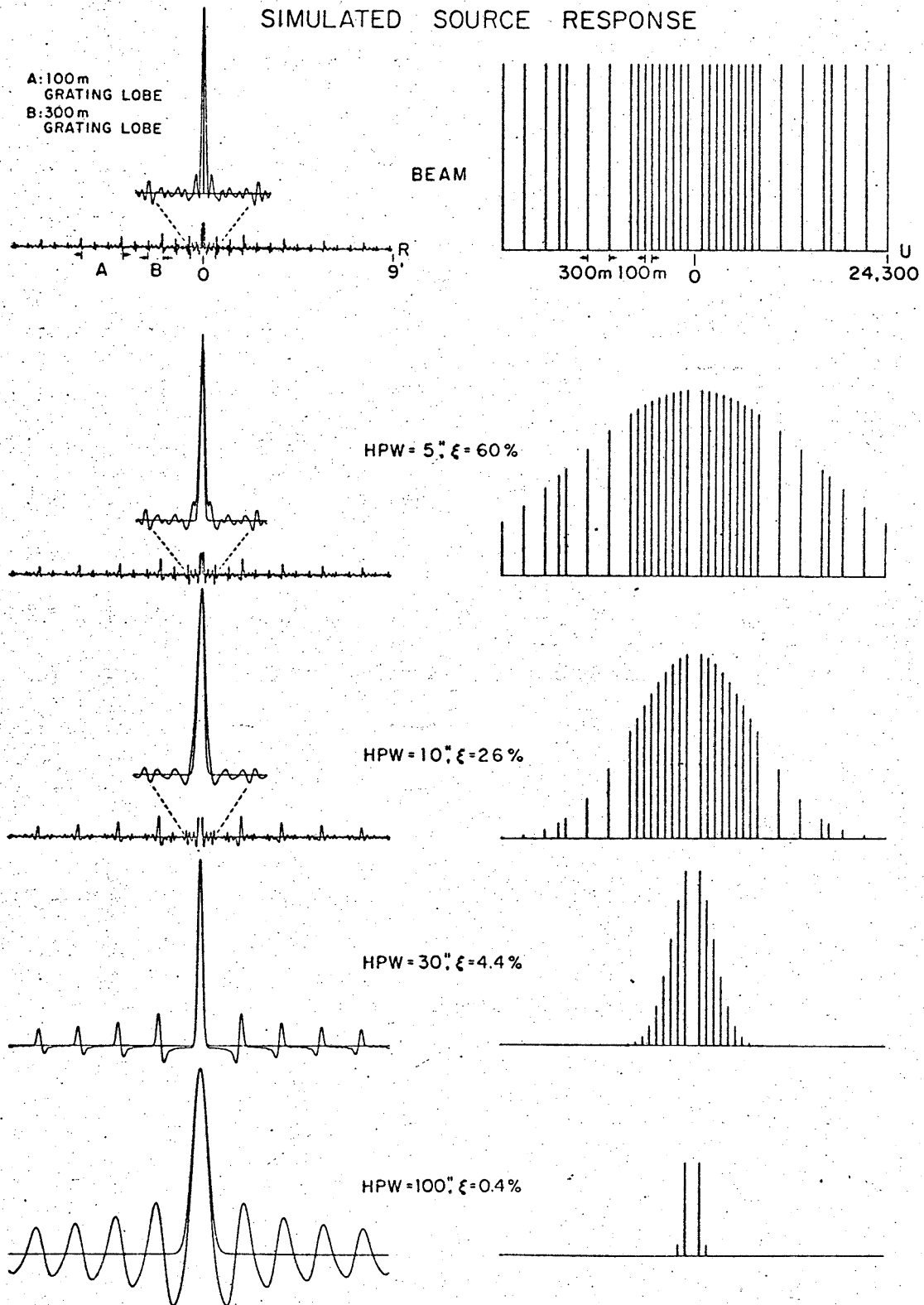


Figure II.11. The interferometer response to Gaussian sources of the widths (HPW) indicated. The true, as well as the observed brightness distribution is shown.  $\xi$  is explained in the text.

of the extended sources reflect this effect. Note also that if small and extended sources of comparable flux exist in the same region, then the extended source may easily be rendered unobservable by the sidelobes of greater brightness associated with the small source. It is apparent that the aperture synthesis technique is best suited for the study of small structure in spite of the fact that the larger structure may account for a major portion of the total source flux. Lastly, note the sidelobe periodicity (indicated by "A" and "B" in the beam response). This behavior reflects the large number of 100 and 300-meter sampling intervals which result from the possible configurations of the NRAO interferometer.

### C. THE REAL INTERFEROMETER

In practice many of the assumptions we made concerning the idealized interferometer are not valid. We therefore relax some of these assumptions in this section. It will be seen that the basic interferometric response described in the preceding sections is not substantially modified. We consider the following:

1. Non-identical apertures and front ends;
2. Sources larger than the primary antennae beams;
3. Non-monochromatic source and delay systems; and
4. Non-incoherent radiation and single vs double side-band interferometry.

If a full treatment is beyond the scope of this discussion, references will be given.

#### 1. Non-identical Apertures and Front Ends

For a discussion of non-identical apertures we begin the discussion with a consideration of the output voltages of Telescopes 1

and 2 as in the first section of this chapter. Let  $A_1$  and  $A_2$  be the effective areas of the antennae, and let the power gains of each telescope be  $G_1$  and  $G_2$ . Then the voltage outputs of the front ends are

$$V_1 = \sqrt{\frac{1}{2} A_1 G_1} \epsilon \cos \left( 2\pi \frac{c}{\lambda} t \right)$$

$$= V_{01} \cos (2\pi ft)$$

$$V_2 = \sqrt{\frac{1}{2} A_2 G_2} \epsilon \cos (2\pi ft + \phi)$$

$$= V_{02} \cos (2\pi ft + \phi).$$

Then  $V_0^2$  in the subsequent discussion of Section A can be replaced by

$$V_0^2 = \frac{1}{2} \sqrt{A_1 A_2} \sqrt{G_1 G_2} \epsilon^2.$$

It is obvious that the interferometer effective area  $A$  is  $\sqrt{A_1 A_2}$  and its gain  $G$  is  $\sqrt{G_1 G_2}$ . As usual, the source flux  $S \propto \epsilon^2$ . Note that if the source is monochromatic, as we have assumed so far, the bandwidth is irrelevant.

## 2. Sources Larger Than the Primary Beams

Since the source to be synthesized can be considered to be the true source distribution  $T(x,y)$  modulated by the primary response pattern  $a(x,y)$ , then  $T(x,y)$  can be replaced with  $t(x,y) = a(x,y) \cdot T(x,y)$  in all equations of Section B of this chapter. In practice,  $a(x,y)$  may be smaller than the beam pattern of the antennae if delays are not properly inserted into the system (see below).

### 3. Non-monochromatic Sources and Delay Systems

It is now appropriate to relax the assumption of monochromaticity. If we receive radiation over a range of frequencies, then the interferometer response can be visualized as a series of lobe combs, one for each frequency. The net response is the sum of the responses of all lobe combs. It is clear that the lobe separation differs slightly at each frequency. Hence the resulting interference between the lobe combs tends to reduce the interferometer response unless all can be aligned so as to interfere constructively in the direction of the source being observed. The problem is exactly analogous to the case of "white light" interference in optics.

Constructive interference between the lobe combs is achieved by inserting delays into the IF path of one of the telescopes as the source moves through the sky. The reasons for this can be most readily understood by the optical "white light" interference analogue. Refer to Figure II.12. The intensity of the interference fringes will be a maximum along a line joining the source and the slit center, i.e., the vector  $\underline{s}$ . In this general direction the fringes are white; the white light fringes are said to exist within the "white light" lobe (see Figure II.13). We show below that the width of this modulation lobe is entirely dependent on the observing bandwidth and is not related to the baseline, source position, etc.

In order to keep the white-light lobe fixed while the source moves across the sky, it is necessary to insert a changing compensating delay  $\Delta t$  which maintains a constant optical path length from the interferometer to the viewing screen. Because this is done in

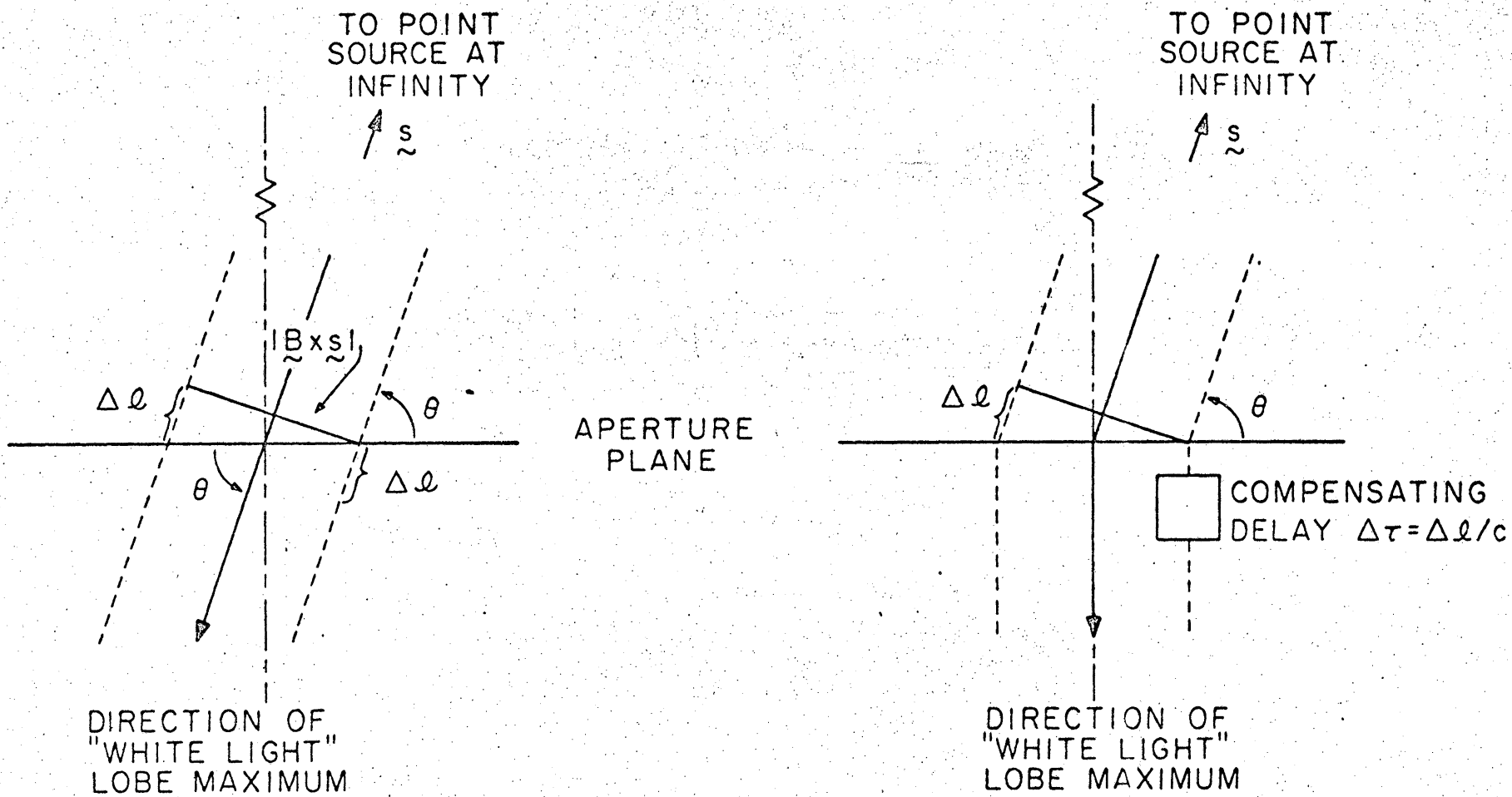


Figure II.12. Geometry pertinent to a discussion of finite bandwidth interferometry. See text.

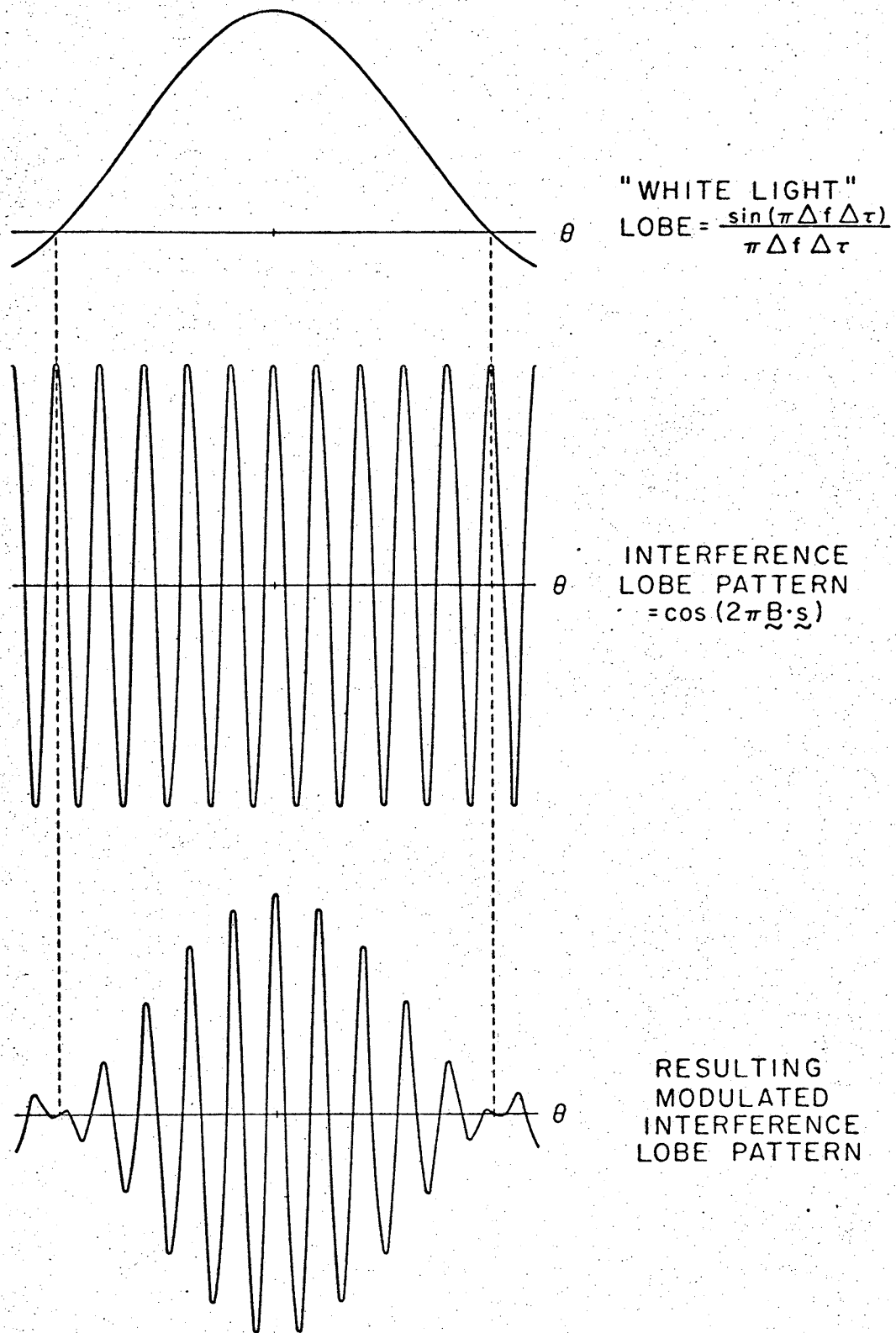


Figure II.13. Response of an interferometer to a source observed with a finite bandwidth  $\Delta f$ . The "white lobe" results from the bandwidth and must be made to track the source by varying  $\Delta\tau$ . The interference lobe pattern is stationary on the sky.

such a manner that the source-baseline geometry is not altered, only the white-light lobe, and not the interference lobes, is kept stationary. Along the viewing screen, then, the interference lobes move as the source changes its position, whereas the white-light lobe stays fixed. (That is, the output of a "photocell" fixed along the optical axis of the interferometer (at the center of the white-light lobe) would be the usual quasi-sinusoidal fringes for the moving source.)

We now redevelop equation II.1 for the case of a finite bandwidth. Refer to Figure II.1. We insert a delay  $\Delta\tau$  into the IF cable following Telescope 1. Then the voltage output per frequency interval of the telescope is

$$dV_1/df = V_0(f) \cos \{2\pi f_{IF}(t+\Delta\tau)\}, \text{ and}$$

$$dV_2/df = V_0(f) \cos \{2\pi f_{IF}t + B \cdot \frac{s}{\lambda}\}.$$

These voltages are then multiplied. Since  $\cos(A+B) \cos(A+C) = \frac{1}{2} \{\cos(2A+B+C) + \cos(B+C)\}$ , we derive

$$dM/df = \frac{1}{2} V_0^2(f) [\cos \{2\pi(f_{IF}\Delta\tau + B \cdot \frac{s}{\lambda})\} + \cos \{2\pi f_{IF}(t+\Delta\tau) + 2\pi B \cdot \frac{s}{\lambda}\}].$$

Again, we reject the second term by the low-pass filter. Then the average response over the bandwidth is

$$R = \frac{1}{\Delta f} \int_{-\infty}^{\infty} \frac{dR}{df} df = \frac{V_0^2}{\Delta f} \int_{-\infty}^{\infty} \cos 2\pi(B \cdot \frac{s}{\lambda} + f\Delta\tau) w(f) df$$

where  $w(f)$  is the bandpass response. Assuming a rectangular bandpass of width  $\Delta f$ , it is easy to show that

$$(II.8) \quad R \propto \frac{\sin(\pi \Delta f \Delta \tau)}{\pi \Delta f \Delta \tau} \cos(2\pi \mathbf{B} \cdot \mathbf{s}).$$

The first term of II.8 is the equation of the white-light lobe (delay pattern). Examples of actual delay patterns are shown in Figure II.14. In general, this lobe is the Fourier transform of the bandpass function. This term modulates the interference lobes in exactly the same manner as the primary antenna beams. In general, the "delay beam" must be made to "track" the source by the insertion of delays sufficiently often so that the delay and the primary beams remain coincident. For the NRAO interferometer, the necessary delays are inserted by an on-line computer once each second in steps as small as 2 nanoseconds.

Because bandwidth effects can be separated from considerations of source baseline geometry and source structure, these effects do not change the fundamental response characteristics of the interferometer described in the first two sections. In the discussion which follows, we generally revert to the assumption of monochromaticity except when the effects of the bandwidth or delays cannot be ignored.

#### 4. Non-incoherent Radiation and Single vs Double Sideband Systems

A discussion of these topics is beyond the scope of this chapter. A full treatment can be found in Read (1963) and Swenson and Mathur (1968). As with the delays, neither problem changes any of the principles of interferometry developed thus far.

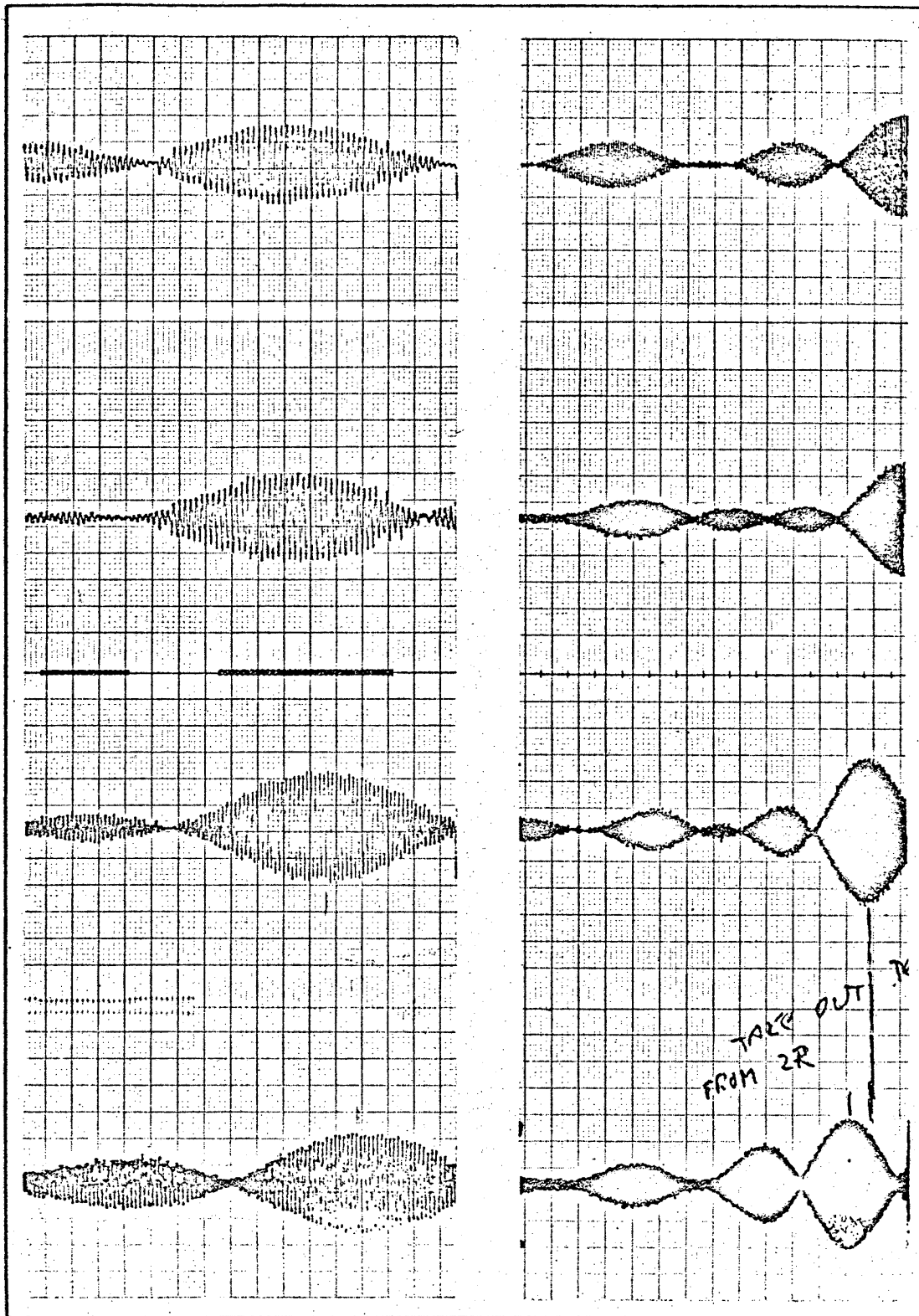


Figure II.14. Examples of actual delay patterns.

#### D. ERROR ANALYSIS

We next consider the sources of errors and noise, the calibrations which reduce the systematic noise, and the effects of noise on the final maps. We shall restrict ourselves to a discussion of these problems as they affect the data at the time of observation. There are additional sources of systematic noise which results from the manner in which the data is processed. These other types of noise are investigated in the last section of this chapter.

The major sources of noise in the amplitudes and phases fall into three major categories: (1) random errors, (2) pseudo-random errors (short duration noise), and (3) systematic errors. Many of the errors have analogies with single dish errors with which it will be assumed the reader is familiar. Other types of errors, most notably those arising because of the atmosphere, would be necessary for single-dish telescopes if they were several kilometers in diameter. Where possible, the analogies are relied upon heavily.

(1) Random errors. The dominant source of truly random error derives from the finite receiver temperature,  $T_r$ . The noise introduced into the fringe signal is given by

$$\Delta T_{\text{rms}} = \gamma T_r / \sqrt{\Delta f \tau} \quad (\gamma \sim \sqrt{2})$$

$T_r$  is nominally 90° K at  $\lambda 11.1$  cm and 125° K at  $\lambda 3.7$  cm. In addition to receiver noise, however, are other sources of noise such as cable losses, antenna spillover, etc., which effectively increase  $T_r$  by 60-70 percent. Hence the noise in the fringe amplitudes is of

order  $0.08^\circ \text{ K}$  at 2.7 GHz and  $0.12^\circ \text{ K}$  at 8.1 GHz after a 30 second integration period (the cycle time of the on-line computer). Normally the fringes are calibrated in units of flux rather than temperature. Since  $\Delta S_{\text{rms}} = 2k/A_e \cdot \Delta T_{\text{rms}}$ , the noise after 30 seconds is 80 m.f.u. and 120 m.f.u. at 2.7 and 8.1 GHz, respectively. Here,  $k$  is the Boltzmann constant,  $A_e$  is the effective area of the antenna ( $A_e = 309 \text{ m}^2$ ), and  $1 \text{ m.f.u.} = 10^{-3} \text{ f.u.} = 10^{-29} \text{ watts m}^{-2} \text{ Hz}^{-1}$ .

(2) Pseudo-random errors (short duration noise). For strong sources, the major source of spurious behavior in the amplitudes and phases arises from instabilities in the atmospheric water vapor. Such variations are called pseudo-random noise because their duration is only a few minutes, so that their net effect over the (u,v) plane is much the same as purely random noise.

The index of refraction of water vapor differs slightly from unity. As a result, the radio wavefront can be significantly retarded as it moves through lower portions of the atmosphere where water vapor content is highest. If the water vapor in the line of sight is not the same at each telescope, then the signal in one telescope is retarded with respect to the other by up to 0.1 nanoseconds (or  $\lambda/2$  at  $\lambda 3.7 \text{ cm}$ ), and the interferometer phase changes appropriately (by up to  $\pi$  radians). Hence the retardation can make the difference between constructive and destructive interference.

(3) Systematic errors. There are many types of systematic errors inherent in interferometry. The most important of these include baseline miscalibration and time-dependent instrumental performance changes which are discussed below. Of secondary importance

are gain variations caused by the insertion loss of delays, smoothing of the fringes by time constants in the analogue equipment, variations of fringe phase across the 30-second integration period, precession, nutation, and aberration of the source position, and systematic atmospheric effects. The atmospheric terms include correction for extinction, refraction, and retardation for an assumed ideal atmosphere. The secondary errors are considered minor, not because they are negligible, but because corrections for their effects are relatively easy to determine. Quite often the effects of systematic errors can be calibrated and corrections can be applied.

We now consider how changes in the instrumental response are determined. System changes, as in the case of a single-dish telescope, are monitored by observations of calibration sources with well-determined positions (invariably point sources). The fringe amplitudes are calibrated by reference to the calibrator flux. Any slowly varying phase changes introduced by the electronics can be determined since the phase of the calibration sources must be zero. For this purpose, it is generally necessary to observe a calibration source approximately every hour.

In addition, we consider the problem of determining the aperture shape, i.e., baseline calibration. For a single-dish telescope, it is generally taken for granted that the aperture is shaped to an accuracy of  $\sim 0.1\lambda$  or better. Random deviations larger than this amount tend to defocus the radiation at the feed, resulting in a reduced aperture efficiency. On the other hand, systematic deviations of the dish surface will shift the focus center away from

from the telescope axis resulting in an apparent source position error (which can be compensated by adjusting the telescope pointing direction or feed position).

The analogous problem in interferometry is to determine the aperture configuration on the ground to an accuracy  $\sim 0.1\lambda$ . Since the telescopes are stationary, the aperture is not affected by random deviations. However, the systematic phase behavior resulting from baseline miscalibration produce effects on the final map much like source position errors. We now elaborate.

If  $\Delta B$  and  $\Delta s$  are baseline and source position errors, then

$$2\pi B \cdot s + \phi = 2\pi (B + \Delta B) \cdot (s + \Delta s),$$

or to first order,

$$\phi \approx 2\pi (B \cdot \Delta s + \Delta B \cdot s).$$

Since  $\Delta s$  is assumed to be zero, we derive

$$\phi = B_x \cos \delta \cos H + \Delta B_y \cos \delta \sin H + \Delta B_z \sin \delta.$$

By sufficient hour angle and declination coverage, a least squares solution for  $\Delta B_x$ ,  $\Delta B_y$ , and  $\Delta B_z$  is possible. In this manner, the baseline can be determined to an accuracy which is generally less than  $0.05\lambda$  at  $111.1$  cm (and three times as much as  $13.7$  cm).

The phase behavior corresponding to a baseline error has much the same form as for source position errors. It is easy to show that the major effect of baseline miscalibration,  $\delta B$ , is much the same as a shift in the apparent source position,

$\delta s \sim \delta B/B$ . Thus if the baseline is  $10^4 \lambda$  and  $\delta B \sim 0.1\lambda$ , then

$\delta s \sim 10^{-5}$  rad  $\sim 2''$  arc. If random baseline errors are made on all baselines, then the displacements  $\delta s$  add up in a random fashion. The source will appear "smeared", although its brightness centroid will be very close to the true position. It is assumed that  $\delta s$  is smaller than the observed source size; if it is not, then the source will appear entirely "washed out".

One good measure of the effects of noise and the success of the calibrations is given by the repeatability of the observations. In Figure II.10 are shown five minute averages of six independent observations of the same source on a baseline of 1900 meters. The data were taken in the summer when atmospheric noise is a maximum. Also shown are the vector average amplitude and phase. It can be seen that the vector average amplitudes are less than the arithmetic averaged amplitudes, particularly in the noisier observations at 8.1 GHz. (Hence, for strong sources, arithmetic amplitude averages help reduce the effects of noise.) The repeatability of the phases, although poorer at  $\lambda 3.7$  cm than at  $\lambda 11.1$  cm, is sufficient in both cases to construct accurate maps. This conclusion is based on maps of calibration sources made from observed data, as compared to maps constructed from a model point source whose  $(u,v)$  coverage is identical.

#### E. CONSTRUCTING AND INTERPRETING THE MAPS

Once a complete set of fully calibrated amplitudes and phases is available, the data can be Fourier transformed to obtain a map of the source brightness distribution. Although a straightforward Fourier transform is possible, it is a time-consuming process

even in a fast computer. An approximate but very fast transform can be obtained by the Cooley-Tukey algorithm. Essentially, this process involves the division of the  $(u,v)$  plane into discrete cells of an appropriate size. The various amplitudes and phase which fall within the cell are all averaged together and treated as one single observation at the cell center. Unsamped cells are assigned a value of zero. Consequently the map of  $T(x,y)$  is computed as a discrete sum over the sampled  $(u,v)$  cells.  $T(x,y)$  is represented as an array of numbers evaluated over a square region of the sky.

It is not the purpose of this discussion to describe the method of all the problems associated with its use. We discuss only those aspects of the procedure which can affect the maps. Our aim is only to provide a sufficient background for proper interpretation of the maps. In this context, we later investigate the problems associated with calibrating the map in physical units. No strong attempt is made to relate the various problems to each other since to do so would involve a lengthy discussion.

The size of the cells in the  $(u,v)$  plane must be chosen so that no structure in the map plane is suppressed. We note that only that structure whose phase variations change appreciably through a  $(u,v)$  cell is affected; this is the structure from the outer regions of the map. That is, the field of view determines the  $(u,v)$  cell size. Since little radiation can be detected outside the primary antenna pattern, the primary beam size sets the  $(u,v)$  cell size. From the sampling theory, the cell size  $(\Delta u, \Delta v)$  is given by

$$(\Delta u, \Delta v) \lesssim \left( \frac{1}{2X}, \frac{1}{2Y} \right),$$

where X and Y are the maximum sizes of interest on the maps; certainly X and Y are not chosen larger than the primary beam dimensions ( $\sim 25.6$  meters/ $\lambda$  for the NRAO interferometer).

The size of the whole (u,v) plane, (U,V), must be chosen to include the synthesized aperture (see Figure II.7). For the NRAO interferometer, the maximum spacing is 2700 meters/ $\lambda$ , or  $\sim 25,000\lambda$  at 2695 MHz and  $75,000\lambda$  at 8085 MHz. Remembering that the aperture is contained in a region extending from (-U,-V), to (U,V), it follows that the total number of cells required in the u and v directions is given by

$$N = \max \left( \frac{2U}{\Delta u}, \frac{2V}{\Delta v} \right).$$

For the NRAO instrument,  $N \sim \frac{2 \times 2700 \text{ m}}{25.6 \text{ m}} = 211$ . For convenience, a  $256 \times 256$  transform is used. A larger transform is not performed because of limitations in the available computer.

The data is sorted and averaged on a cell-by-cell basis. The amount of data averaged into each cell is proportional to the time required to transverse a cell. This time is not uniform over the entire plane; the traversal time per cell varies from  $\sim 2$  minutes to almost an hour. Generally, more cells are traversed per unit time for the outer spacings and near crossover (see Figure II.7). Therefore, the noise in each cell varies over the (u,v) plane. Nonetheless, each cell is weighted equally in the Cooley-Tukey algorithm. The net effect is that noise tends to be larger in N-S directions on the map, particularly for sources at low declination. It is found that the exclusion of the noisier data often helps clean up the map. In fact, it is standard procedure to modulate the data, once it has been arranged in the (u,v)

plane, by a unit height Gaussian which falls to a value of 0.30 at the outermost baseline. The modulation is chosen since signal intensities tend to decrease and atmospheric noise tends to increase on the long spacings.

As mentioned above, all data averaged into a cell is implicitly assumed by the algorithm to have been observed at the cell center. Consequently it is possible to shift the actual values of  $u$  and  $v$  assigned to the data by up to half the diagonal length of the cell. In general, provided the cell size is chosen properly, the resulting distortion is unimportant since the shift of  $u$  and  $v$  is small compared to their absolute magnitude. This is not the case, however, for data near the  $(u,v)$  origin. Consequently, it is possible to expect that the large-scale structure might be distorted.

Once the map is made (generally in the form of a contour map), it is necessary to establish a scale in physical units if interpretation is to be attempted. However, the calibration of the map is extremely difficult. This conclusion follows from the incomplete sampling of the  $(u,v)$  plane which leads to the complex sidelobe response.

The flux of point sources can be established by comparison of its peak response temperature to that of a point source of a known flux. However, it is very important that the known point source be sampled in the  $(u,v)$  plane in exactly the same manner as the source being studied. In general, this means that the comparison source must have exactly the same declination. Since this situation is rare, it is easiest to construct a model comparison source having the identical  $(u,v)$  coverage.

For the present study, it cannot be established that any of the structure is small compared to the synthesized beam size. As a result, we consider other methods used to estimate the flux of extended sources. There are two common methods. These include point by point integration of the brightness temperature and model fitting. The former method is not accurate over the entire map since it is known a priori that the sum of the temperatures is zero (see Section B, this chapter). Crude estimates can be obtained by restricting the integration to a region inside the sidelobes. However, a glance at Figure II.11 is a convincing argument that such a procedure is most inaccurate when sources of different sizes or intensities appear within the sidelobes of each other.

One common method of determining the observed source parameters involves the fitting of models to the data. Generally, model fitting involves the subtraction of simple sources from the map until the map structure disappears. In practice, such a procedure is quite laborious, and the ability of the model to converge is very sensitive to observational noise and sampling inadequacies. In the past, models have been fit by several authors (Webster and Altenhoff, 1970a, 1970b; Wynn-Williams, 1971). There is no conclusive evidence that the models they fit are unique. Furthermore, even though their results are internally consistent, it will be seen in the following chapter that the values of the physical parameters they derive do not justify the labor involved.

Therefore, no attempt is made to derive accurate fluxes in the present study. Crude estimates must suffice. For this, a fairly reliable physical scale for the brightness temperatures will be

estimated by comparison to the peak response of model point sources for each map. The response to these point sources is given along with each map. However, little emphasis is placed on values of physical parameters estimated from the absolute brightnesses of the maps.

Instead, estimates of the physical parameters are based on the spectral behavior of the structure between  $\lambda 11.1$  cm and  $\lambda 3.7$  cm. Such a procedure is accurate because the maps can be constructed from subsets of the available data at these frequencies whose distribution in the  $(u,v)$  plane is identical. Consequently, the ratio of brightness of the two frequencies is very accurately determined. The method is explained in detail in the next chapter.

In this chapter we have discussed how the interferometer responds to sources of different structure. It has been shown how the brightness distribution of a source can be reconstructed from parameters which describe the interferometer response, i.e., the fringes. The sources of error have been discussed in regards to their effect on the observations and the maps. Finally, some of the problems associated with making and interpreting the maps have been considered.

## REFERENCES

Road, R. B. 1963, Ap. J., 138, 1.

Swenson, G. W., Jr. and Mathur, N. C. 1968, Proc. IEEE, 56, 12.

Webster, W. J. and Altenhoff, W. J. 1970a, Astrophys. Letters, 5, 233.

———. 1970b, A. J., 75, 896.

Wynn-Williams, C. G. 1971, M.N.R.A.S., 151, 397.